

Accelerated Article Preview

Sulphur dioxide in the mid-infrared transmission spectrum of WASP-39b

Received: 11 August 2023

Accepted: 5 January 2024

Accelerated Article Preview

Cite this article as: Powell, D. et al. Sulphur dioxide in the mid-infrared transmission spectrum of WASP-39b. *Nature* <https://doi.org/10.1038/s41586-024-07040-9> (2024)

Diana Powell, Adina D. Feinstein, Elspeth K. H. Lee, Michael Zhang, Shang-Min Tsai, Jake Taylor, James Kirk, Taylor Bell, Joanna K. Barstow, Peter Gao, Jacob L. Bean, Jasmina Blecic, Katy L. Chubb, Ian J. M. Crossfield, Sean Jordan, Daniel Kitzmann, Sarah E. Moran, Giuseppe Morello, Julianne I. Moses, Luis Welbanks, Jeehyun Yang, Xi Zhang, Eva-Maria Ahrer, Aaron Bello-Arufe, Jonathan Brande, S. L. Casewell, Nicolas Crouzet, Patricio E. Cubillos, Brice-Olivier Demory, Achrène Dyrek, Laura Flagg, Renyu Hu, Julie Inglis, Kathryn D. Jones, Laura Kreidberg, Mercedes López-Morales, Pierre-Olivier Lagage, Erik A. Meier Valdés, Yamila Miguel, Vivien Parmentier, Anjali A. A. Piette, Benjamin V. Rackham, Michael Radica, Seth Redfield, Kevin B. Stevenson, Hannah R. Wakeford, Keshav Aggarwal, Munazza K. Alam, Natalie M. Batalha, Natasha E. Batalha, Björn Benneke, Zach K. Berta-Thompson, Ryan P. Brady, Claudio Caceres, Aarynn L. Carter, Jean-Michel Désert, Joseph Harrington, Nicolas Iro, Michael R. Line, Joshua D. Lothringer, Ryan J. MacDonald, Luigi Mancini, Karan Molaverdikhani, Sagnick Mukherjee, Matthew C. Nixon, Apurva V. Oza, Enric Palle, Zafar Rustamkulov, David K. Sing, Maria E. Steinrueck, Olivia Venot, Peter J. Wheatley & Sergei N. Yurchenko

This is a PDF file of a peer-reviewed paper that has been accepted for publication. Although unedited, the content has been subjected to preliminary formatting. Nature is providing this early version of the typeset paper as a service to our authors and readers. The text and figures will undergo copyediting and a proof review before the paper is published in its final form. Please note that during the production process errors may be discovered which could affect the content, and all legal disclaimers apply.

Sulphur dioxide in the mid-infrared transmission spectrum of WASP-39b

Diana Powell^{1,2*}, Adina D. Feinstein^{2,3}, Elspeth K. H. Lee⁴, Michael Zhang^{2,5}, Shang-Min Tsai⁶, Jake Taylor^{7,8}, James Kirk⁹, Taylor Bell^{10,11}, Joanna K. Barstow¹², Peter Gao¹³, Jacob L. Bean², Jasmina Blecic^{14,15}, Katy L. Chubb¹⁶, Ian J. M. Crossfield¹⁷, Sean Jordan¹⁸, Daniel Kitzmann³, Sarah E. Moran¹⁹, Giuseppe Morello^{20,21,22}, Julianne I. Moses²³, Luis Welbanks^{24,25}, Jeehyun Yang²⁶, Xi Zhang²⁷, Eva-Maria Ahrer^{28,29}, Aaron Bello-Arufe³⁰, Jonathan Brande¹⁷, S. L. Casewell³¹, Nicolas Crouzet³², Patricio E. Cubillos^{33,34}, Brice-Olivier Demory^{4,35}, Achrène Dyrek³⁶, Laura Flagg³⁷, Renyu Hu^{30,38}, Julie Inglis³⁸, Kathryn D. Jones⁴, Laura Kreidberg³⁹, Mercedes López-Morales¹, Pierre-Olivier Lagage³⁶, Erik A. Meier Valdés⁴, Yamila Miguel^{32,40}, Vivien Parmentier⁴¹, Anjali A. A. Piette¹³, Benjamin V. Rackham^{42,43,5}, Michael Radica⁸, Seth Redfield⁴⁴, Kevin B. Stevenson⁴⁵, Hannah R. Wakeford⁴⁶, Keshav Aggarwal⁴⁷, Munazza K. Alam¹³, Natalie M. Batalha⁴⁸, Natasha E. Batalha⁴⁹, Björn Benneke⁸, Zach K. Berta-Thompson⁵⁰, Ryan P. Brady⁵¹, Claudio Caceres^{52,53,54}, Aarynn L. Carter⁴⁸, Jean-Michel Désert⁵⁵, Joseph Harrington⁵⁶, Nicolas Iro⁵⁷, Michael R. Line²⁴, Joshua D. Lothringer⁵⁸, Ryan J. MacDonald^{59,25}, Luigi Mancini^{60,33,39}, Karan Molaverdikhani^{61,62}, Sagnick Mukherjee⁴⁸, Matthew C. Nixon⁶³, Apurva V. Oza³⁰, Enric Palle²¹, Zafar Rustamkulov⁶⁴, David K. Sing^{64,65}, Maria E. Steinrueck³⁹, Olivia Venot⁶⁶, Peter J. Wheatley^{28,29} and Sergei N. Yurchenko⁵¹

*Corresponding author(s). E-mail(s): diana.powell@uchicago.edu

All author affiliations are listed at the end of the paper.

Abstract

The recent inference of sulphur dioxide (SO_2) in the atmosphere of the hot (~ 1100 K), Saturn-mass exoplanet WASP-39b from near-infrared JWST observations (1–3) suggests that photochemistry is a key process in high temperature exoplanet

2 *Mid-Infrared Spectrum of WASP-39b*

34 atmospheres (4). This is due to the low (<1 ppb) abundance of
35 SO_2 under thermochemical equilibrium, compared to that pro-
36 duced from the photochemistry of H_2O and H_2S (1–10 ppm)
37 (4–9). However, the SO_2 inference was made from a single,
38 small molecular feature in the transmission spectrum of WASP-
39 39b at 4.05 μm , and therefore the detection of other SO_2
40 absorption bands at different wavelengths is needed to better
41 constrain the SO_2 abundance. Here we report the detection
42 of SO_2 spectral features at 7.7 and 8.5 μm in the 5–12 μm
43 transmission spectrum of WASP-39b measured by the JWST
44 Mid-Infrared Instrument (MIRI) Low Resolution Spectrome-
45 ter (LRS) (10). Our observations suggest an abundance of SO_2
46 of 0.5–25 ppm (1σ range), consistent with previous findings
47 (4). In addition to SO_2 , we find broad water vapour absorp-
48 tion features, as well as an unexplained decrease in the transit
49 depth at wavelengths longer than 10 μm . Fitting the spectrum
50 with a grid of atmospheric forward models, we derive an atmo-
51 spheric heavy element content (metallicity) for WASP-39b of
52 $\sim 7.1\text{--}8.0 \times$ solar and demonstrate that photochemistry shapes
53 the spectra of WASP-39b across a broad wavelength range.

54 We observed WASP-39b using JWST MIRI/LRS on UTC 2023-02-14 from
55 15:03:20 to 22:59:36, spanning a total of 7.94 hours (Director’s Discretionary
56 Time PID 2783). The observation included the full 2.8-hour transit, as well as
57 3 hours before and 1.87 hours after the transit to measure the stellar baseline.
58 We used the slitless prism mode with no dithering. In this mode, MIRI/LRS
59 yields a spectral range from 5–12 μm , at an average resolving power of $R \equiv$
60 $\lambda/\Delta\lambda \approx 100$, where λ is the wavelength. The time-series observations included
61 1779 integrations of 16 seconds (100 groups per integration). No region of the
62 detector was saturated.

63 We extracted the time-series stellar spectra using three independently
64 developed reduction pipelines to test the impact of background modelling,
65 spectral extraction method and aperture width, and light-curve-fitting routines
66 on the resulting planetary transmission spectrum (see Methods and Extended
67 Data Figures 1 and 2). We summed across the extracted stellar spectra to
68 create white-light curves (Extended Data Figure 2) as well as binned spec-
69 tral photometric light curves for each pipeline (Figure 1). The light curves show
70 clear instrumental systematics at the beginning of the observation that are
71 driven by a decreasing exponential ramp effect (11). At the detector level, the
72 observations showed correlations with spatial position and an odd–even effect
73 from row to row due to the readout time (12). We do not see evidence of a
74 very sharp, strong change in the initial exponential ramp’s sign, amplitude, or
75 timescale, known as a “shadowed region”, in our observations (Extended Data
76 Figure 1; 13). We use wide spectral photometric light curve bins of $\Delta\lambda = 0.25\mu\text{m}$
77 to average over the odd–even row effect (13) and we note that our conclusions

78 are insensitive to the chosen bin size (smaller bins of $0.15\text{ }\mu\text{m}$ derive the same
 79 results) as well as the choice of the origin binning wavelength.

80 We present the resulting transmission spectrum from each pipeline in
 81 Figure 2. Within the spectra, we are able to identify two broad absorption
 82 features belonging to SO_2 at 7.7 and $8.5\text{ }\mu\text{m}$, which correspond to the asym-
 83 metric ν_3 and symmetric ν_1 fundamental bands, respectively, consistent with
 84 predictions from photochemical models (4). We are also able to discern H_2O
 85 absorption, although it is mostly apparent between 5 and $7\text{ }\mu\text{m}$ owing to the
 86 overlapping SO_2 feature at longer wavelengths. There is an abrupt decrease
 87 in the transit depth at $\lambda = 10\text{ }\mu\text{m}$. The shadowed region systematic occurs
 88 from $\lambda \geq 10.6 - 11.8\text{ }\mu\text{m}$ (13), at longer wavelengths compared to the abrupt
 89 decrease in the transmission spectrum. Therefore, if this abrupt change arose
 90 from the instrument and is not of astrophysical origin, then it is most likely
 91 driven by a different source of detector noise or an artifact that is not currently
 92 well understood.

93 In order to determine the detection significance of SO_2 in our data and con-
 94 strain its abundance, we conducted seven independent Bayesian retrievals on
 95 each of the three data reductions. Each nominal retrieval includes SO_2 and H_2O
 96 as spectrally active gases, as well as a variety of cloud and haze treatments to
 97 account for degeneracies between retrieved cloud/haze properties and molec-
 98 ular abundances (see Methods). Other spectrally active gases were initially
 99 tested by the retrievals, including CH_4 , NH_3 , HCN , CO , CO_2 , C_2H_2 , H_2S , but
 100 none of them showed significant detections. As shown in Figure 3 and Extended
 101 Data Table 4, the fits of the retrieval models to the data are generally good,
 102 with reduced chi-squared values close to 1. SO_2 is detected to at least $\sim 3\sigma$ sig-
 103 nificance for all retrieval frameworks and data reductions, except for one single
 104 retrieval–data reduction combination with a 2.5σ detection, where other free
 105 parameters slightly reduced the SO_2 detection significance (see Methods). We
 106 retrieve a range of log volume mixing ratios from -6.3 to -4.6 (0.5 – 25 ppm; low-
 107 est to highest 1σ uncertainty bounds across all 6 retrieval frameworks) for the
 108 Eureka! reduction. Retrievals for the other reductions yielded similar results
 109 and are discussed in Methods and shown in Extended Data Figure 4.

110 Similar to SO_2 , the retrieved H_2O abundances are largely consistent across
 111 all retrievals and reductions (see Extended Data Table 4 and Extended Data
 112 Figure 4), although the spread of values for the detection significance is greater
 113 than for SO_2 , with some reduction-retrieval combinations yielding $\lesssim 2\sigma$ while
 114 for others it is above 5σ . This serves to highlight the impact of choices made
 115 at both the reduction and retrieval stages on conclusions drawn from a spec-
 116 trum. We postulate that the variation in detection significance that we see
 117 is due to the fact that the H_2O feature present in this observation is fairly
 118 broad, and likely impacted by the stronger SO_2 feature at longer wavelengths
 119 and modelled haze properties at shorter wavelengths. For the Aurora/Eureka!
 120 combination the water abundance is relatively poorly constrained, with long
 121 tails in the distribution towards lower abundances and haze compensating for
 122 the relative lack of H_2O absorption at short wavelengths. Across the other six

4 Mid-Infrared Spectrum of WASP-39b

123 retrievals for the Eureka! reduction, the retrieved range of log volume mixing
124 ratios is from -2.4 to -1.2 (0.4–6.3%; lowest to highest 1σ uncertainty).

125 In addition to SO_2 and H_2O , one retrieval framework found weak-to-
126 moderate (2.5σ) evidence for SO , with a feature between 8 and 10 μm (see
127 Methods), which is predicted to be present by photochemical models (4; 5),
128 but additional observations would be needed to confirm or rule out its exis-
129 tence. Furthermore, we can largely rule out a grey cloud extending to low
130 pressures with broad terminator coverage (see Methods), but more detailed
131 cloud and haze properties such as particle sizes and cloud top pressure cannot
132 be consistently constrained.

133 We use a suite of independent forward-model grids that include photochem-
134 istry to infer the atmospheric metallicity and elemental ratios of WASP-39b
135 from the observed SO_2 abundance (see Methods). As SO_2 is photochemical
136 in origin, a rigorous treatment of photochemistry is vital for connecting SO_2
137 to bulk atmospheric properties. Figure 4 shows the comparison between four
138 independent photochemical models, all of which include moderately different
139 chemical networks for H, C, O, N, and S molecules and use the same average
140 atmospheric temperature–pressure profiles (morning and evening terminators),
141 eddy diffusion profile, and stellar spectrum of WASP-39 adopted by ref. (4)
142 as inputs. The model transmission spectra generated from the four photo-
143 chemical models are largely consistent with each other and the data, showing
144 that sufficient SO_2 is generated photochemically to explain the 7.7 and 8.5 μm
145 absorption features. In particular, the limb-averaged volume mixing ratio of
146 SO_2 for the best-fitting $7.5\times$ solar metallicity models span the range of 2.5–
147 6.1 ppm, in line with our free-retrieval results (Extended Data Table 4). The
148 8.5 μm SO_2 feature is notably sensitive to metallicity in this range while the
149 strongest 7.7 μm feature starts to saturate with metallicity $\gtrsim 7.5 \times$ solar.

150 Using an expanded grid of one of the photochemical models (see Meth-
151 ods; 14) we find best-fitting atmospheric metallicity values of $7.1\text{--}8.0 \times$ solar
152 across the three data reductions, as well as a consistent – though weak – pref-
153 erence for a super-solar O/S ratio, sub-solar C/O, and approximately solar
154 C/S. Even though no carbon species is detected in the spectrum, constraints
155 on the carbon abundance are still possible through the high degree of cou-
156 pling between the CHONS elements in the photochemistry. These results are
157 largely corroborated by comparisons to independent, self-consistent, radiative-
158 convective-thermochemical equilibrium model grids that are post-processed
159 to include SO_2 (see Methods), which also infer a sub-solar C/O, as well as
160 slightly higher atmospheric metallicity values ranging between $10\text{--}30\times$ solar,
161 depending on the specific data reduction. These findings are within the range
162 of C/O (sub-solar) and atmospheric metallicities (supersolar) derived from
163 near-infrared JWST transmission spectra of WASP-39b using self-consistent
164 radiative-convective thermal equilibrium grid models (1–3; 15; 16) and photo-
165 chemical models that were able to match the near-infrared SO_2 feature (4). Our
166 work therefore shows that JWST’s MIRI LRS is fully capable of producing
167 information-rich exoplanet observations like the near-infrared instruments.

The interpretation of WASP-39b's transmission spectrum at wavelengths beyond 10 μm is uncertain. If the observed sudden drop in transit depth is astrophysical in origin rather than due to an artifact in the data, then several possibilities exist. For example, the transit radius of a planet can decrease quickly with increasing wavelength when a cloud layer becomes sufficiently optically thin such that we can probe below the cloud base (17). In addition, spectral features associated with the vibrational modes of bonds of several cloud and haze species are situated in the mid-infrared (18–20), but none of the known features can explain our data. Meanwhile, the absorption cross sections of some gaseous species, such as metal hydrides (e.g. SiH and BeH), can exhibit downward slopes starting at $\sim 10 \mu\text{m}$ (21). However, the abundances of these species needed to explain the observed feature (~ 1000 ppm) are orders of magnitude greater than what is expected in a near-solar metallicity atmosphere (see Methods). Additional observations will be needed to explore the behavior and provenance of the $>10 \mu\text{m}$ transmission spectrum of WASP-39b.

References

- [1] JWST Transiting Exoplanet Community Early Release Science Team *et al.* Identification of carbon dioxide in an exoplanet atmosphere. *Nature* **614** (7949), 649–652 (2023) .
- [2] Alderson, L. *et al.* Early release science of the exoplanet wasp-39b with jwst nirspec g395h. *Nature* (2023) .
- [3] Rustamkulov, Z. *et al.* Early Release Science of the exoplanet WASP-39b with JWST NIRSpec PRISM. *Nature* **614** (7949), 659–663 (2023) .
- [4] Tsai, S.-M. *et al.* Photochemically produced SO₂ in the atmosphere of WASP-39b. *Nature* **617** (7961), 483–487 (2023) .
- [5] Zahnle, K., Marley, M. S., Freedman, R. S., Lodders, K. & Fortney, J. J. Atmospheric Sulfur Photochemistry on Hot Jupiters. *Astrophys. J.* **701** (1), L20–L24 (2009) .
- [6] Zahnle, K., Marley, M. S., Morley, C. V. & Moses, J. I. Photolytic Hazes in the Atmosphere Of 51 Eri b. *Astrophys. J.* **824** (2), 137–153 (2016) .
- [7] Hobbs, R., Rimmer, P. B., Shorttle, O. & Madhusudhan, N. Sulfur chemistry in the atmospheres of warm and hot Jupiters. *Mon. Not. R. Astron. Soc.* **506** (3), 3186–3204 (2021) .
- [8] Tsai, S.-M. *et al.* A comparative study of atmospheric chemistry with VULCAN. *Astrophys. J.* **923** (2), 264–305 (2021) .
- [9] Polman, J., Waters, L. B. F. M., Min, M., Miguel, Y. & Khorshid, N. H₂S and SO₂ detectability in Hot Jupiters: Sulfur species as indicator of

6 *Mid-Infrared Spectrum of WASP-39b*

205 metallicity and C/O ratio. *arXiv e-prints* arXiv:2208.00469 (2022) .

206 [10] Kendrew, S. *et al.* The Mid-Infrared Instrument for the James Webb
207 Space Telescope, IV: The Low-Resolution Spectrometer. *PASP* **127** (953),
208 623 (2015) .

209 [11] Bouwman, J. *et al.* Spectroscopic Time Series Performance of the Mid-
210 infrared Instrument on the JWST. *PASP* **135** (1045), 038002 (2023)

211 .

212 [12] Ressler, M. E. *et al.* The Mid-Infrared Instrument for the James Webb
213 Space Telescope, VIII: The MIRI Focal Plane System. *PASP* **127** (953),
214 675 (2015) .

215 [13] Bell, T. J. *et al.* A First Look at the JWST MIRI/LRS Phase Curve of
216 WASP-43b. *arXiv e-prints* (2023). [arXiv:2301.06350](https://arxiv.org/abs/2301.06350) .

217 [14] Crossfield, I. J. M. Volatile-to-sulfur Ratios Can Recover a Gas Giant's
218 Accretion History. *ApJL* **952** (1), L18 (2023) .

219 [15] Feinstein, A. D. *et al.* Early Release Science of the exoplanet WASP-39b
220 with JWST NIRISS. *Nature* **614** (7949), 670–675 (2023) .

221 [16] Ahrer, E.-M. *et al.* Early Release Science of the exoplanet WASP-39b
222 with JWST NIRCam. *Nature* **614** (7949), 653–658 (2023) .

223 [17] Vahidinia, S., Cuzzi, J. N., Marley, M. & Fortney, J. Cloud Base Signature
224 in Transmission Spectra of Exoplanet Atmospheres. *ApJL* **789** (1), L11
225 (2014) .

226 [18] Wakeford, H. R. & Sing, D. K. Transmission spectral properties of clouds
227 for hot Jupiter exoplanets. *A&A* **573**, A122 (2015) .

228 [19] Gao, P., Wakeford, H. R., Moran, S. E. & Parmentier, V. Aerosols in Exo-
229 planet Atmospheres. *Journal of Geophysical Research (Planets)* **126** (4),
230 e06655 (2021) .

231 [20] Miles, B. E. *et al.* The JWST Early-release Science Program for Direct
232 Observations of Exoplanetary Systems II: A 1 to 20 μm Spectrum of the
233 Planetary-mass Companion VHS 1256-1257 b. *ApJL* **946** (1), L6 (2023) .

234 [21] Tennyson, J. & Yurchenko, S. The ExoMol Atlas of Molecular Opacities.
235 *Atoms* **6** (2), 26 (2018) .

236 [22] Polyansky, O. L. *et al.* ExoMol molecular line lists XXX: a complete high-
237 accuracy line list for water. *Mon. Not. R. Astron. Soc.* **480** (2), 2597–2608
238 (2018) .

- [23] Underwood, D. S. *et al.* ExoMol molecular line lists - XIV. The rotation-vibration spectrum of hot SO₂. *Mon. Not. R. Astron. Soc.* **459** (4), 3890–3899 (2016).
- [24] Cubillos P. E., B. J. PyratBay Documentation. <https://pyratbay.readthedocs.io/en/latest/> (2021). [Online].

244
245

Fig. 1 A sample of spectrophotometric light curves and residuals for WASP-39b’s transit observed with MIRI/LRS. **a:** An exoplanet transit model multiplied by a systematics model (solid black line) was fitted to each light curve. **b:** The residuals to the best-fit models are shown for each light curve. We report the 1σ scatter in each light curve as the standard deviation of the out-of-transit residuals, with the ratio to the predicted photon noise in parentheses. The reduction is from Eureka!.

253

254

Fig. 2 MIRI/LRS transmission spectra of WASP-39b derived using three independent reduction pipelines. **a:** The spectrum is dominated by broad absorption features from SO₂ at 7.7 and 8.5 μm and H₂O across the entire wavelength coverage of MIRI/LRS. We define our uncertainties as 1σ . **b:** We present the log of opacities of dominant species in the spectrum in units of $\text{cm}^2 \text{ mol}^{-1}$. The opacities were adopted from PLATON using ExoMol line lists (22; 23) and assume atmospheric properties pressure, $P = 1 \text{ mbar}$ and temperature, $T = 1000 \text{ K}$.

263

264

Fig. 3 Free retrievals of the MIRI/LRS transmission spectrum of WASP-39b. **a:** The spectrum from the Eureka! reduction (with 1σ uncertainties) is compared to the best-fit retrieved spectra and associated 1σ shaded regions from six free retrieval codes. **b:** The corresponding posterior probability distributions of the volume mixing ratio (VMR) and associated 1σ uncertainties (points) for the SO₂ abundance. The quoted $\log(\text{SO}_2)$ ranges from the lowest to the highest 1σ bounds of all six posteriors. We chose the Eureka! reduction due to its similar reduction steps to previous WASP-39b observations (2; 3; 15; 16) and the fact that it provides the full wavelength coverage of the observations. Results from the other two reductions for SO₂ give broadly consistent results and are discussed further in Methods.

276

277

Fig. 4 Comparison of four independent photochemical models to the observed MIRI/LRS transmission spectra of WASP-39b. **a:** Comparison of morning and evening limb-averaged theoretical transmission spectra to the observations assuming a best-fit atmospheric metallicity of $7.5 \times \text{solar}$. **b:** Limb-averaged SO₂ VMR between 10 and 0.01 mbar as a function of metallicity for the four photochemical models. The shaded and hatched yellow region

represents the 1σ SO₂ constraint from the free retrievals on the Eureka! reduction (Fig. 3). **c:** Dependence of VULCAN modeled transmission spectrum on atmospheric metallicity, as compared to the Eureka! reduction. The Tiberius reduction prefers a metallicity of $7.5 \times$ solar, while the SPARTA reduction prefers $10 \times$ solar (see Extended Data). The VULCAN models suggest that there is only a minor (< 0.05%) difference expected for the SO₂ feature at $7.7\mu\text{m}$ when assuming a higher atmospheric metallicity, while the SO₂ feature at $8.5\mu\text{m}$ is more sensitive to subtle changes. The SO₂ feature at $8.5\mu\text{m}$ is fit well by the $7.5 - 10 \times$ solar metallicity models.

Extended Data Fig. 1 Comparison of the different background modelling and subtraction per each pipeline. (a) A median out-of-transit image of the MIRI/LRS detector from the *jwst* pipeline's Stage 2 processing. (b) Background models from Eureka! (1), Tiberius (2), and SPARTA (3). (c) Background subtracted Stage 2 outputs from each pipeline. The smoothly varying background is expected for MIRI/LRS. There are no discrete features or sharp changes in the background at y-pixels < 244, corresponding to $\lambda = 10\mu\text{m}$, which has been seen in other observations (13). All images are given in Data Numbers per second (DN s⁻¹). The Tiberius reduction did not extract spectra as far red as Eureka! and SPARTA, which is the cause of the horizontal bar in panels b2 and c2.

Extended Data Fig. 2 MIRI/LRS white and spectrophotometric light curves from the three independent reduction pipelines used in this work. (a) We quote the out-of-transit parts-per-million scatter in each light curve in the figure. We define the out-of-transit time as $-0.135 < t [\text{days}] < -0.07$ and $0.07 < t [\text{days}] < 0.14$; these times were selected as they ignore the exponential ramp at the beginning of the observations and do not include any data in transit ingress/egress. (b) The residuals and errors of the data compared to the best-fit transit model. Errors quoted are 1σ . (c) The spectrophotometric light curves are normalized by the out-of-transit flux during the observations. All reductions show consistent out-of-transit scatter in all wavelength bins ($\Delta\lambda = 0.25\mu\text{m}$). The white spaces in c1 are where values in the light curve are NaN.

Extended Data Table 1 The system parameters resulting from the white light curve fits.

Extended Data Table 2 Results from the IDIC grid assuming C, O, and S have the same abundance enhancement relative to Solar (i.e., M*).

330 **Extended Data Table 3** Results from the IDIC grid assuming C, O, and S
331 can take different abundances relative to Solar (C*, O*, S*). χ^2 for the three
332 best-fitting model spectra for each of the three reductions are shown.

333

334

335 **Extended Data Fig. 3** The best-fitting cloudy PICASO grid models
336 (gold lines) are shown with SO₂ (a) and without SO₂ (b) compared
337 to the JWST MIRI/LRS data (black points) from the Eureka! reduc-
338 tion. Also shown are the best-fits with H₂O (dark teal), SO₂ (red), CH₄
339 (light teal), and clouds (navy blue) removed from the model, demon-
340 strating which absorbers dominate the opacity of the best-fit model. When SO₂ is
341 not included in the model, excess CH₄ compensates for its absorption in the
342 Eureka! reduction as shown in the lower panel.

343

344

345 **Extended Data Fig. 4** Retrieved log of SO₂ and H₂O volume mixing
346 ratio (VMR) posteriors from all six retrieval codes and three data
347 reductions. Median values and 1σ uncertainties are given in the coloured
348 points.

349

350

351 **Extended Data Table 4** This table collects all the free retrieval results for
352 H₂O and SO₂ volume mixing ratios, together with their detection significance,
353 and the goodness of fit for each individual retrieval. The cloud model used
354 for each retrieval code is also noted. For the most part, the abundances are
355 consistent between retrieval codes for a given reduction, although there is some
356 variation between reductions.

357 Methods

358 Data Reduction

359 We applied three independent data reduction and light-curve-fitting routines
 360 to the MIRI/LRS observations. Below, we describe the major reduction steps
 361 taken by each pipeline, followed by their light-curve-fitting methodologies.
 362 Additionally, we discuss the differences in the data reduction pipelines that
 363 resulted in differing shapes of the H₂O absorption feature at < 7 μm.

364 Eureka!

365 Initially, nine independent teams performed a reduction of these data using
 366 the open-source **Eureka!**(25) pipeline. From those analyses, we ultimately
 367 chose one analysis to highlight in this paper based on comparisons of the
 368 white and red noise of the residuals after fitting. Our fiducial **Eureka!** reduc-
 369 tion very closely followed the methods developed for the Transiting Exoplanet
 370 ERS team’s MIRI/LRS phase curve observations of WASP-43b and described
 371 in ref.(13; 27). As extensive parameter studies were performed on **Eureka!**’s
 372 Stage 1–3 parameters using the WASP-43b data, the best parameter settings
 373 identified from that work are reused here and are briefly summarized below.
 374 The other **Eureka!** analyses had used different reduction parameters and were
 375 generally consistent with, but noisier than, our fiducial **Eureka!** analyses. The
 376 full **Eureka!** Control Files and **Eureka!** Parameter Files files used in these
 377 analyses are available as part of the data products associated with this work
 378 (<https://doi.org/10.5281/zenodo.10055845>).

379 We made use of version 0.9 of the **Eureka!**(25) pipeline, CRDS version
 380 11.16.16 and context 1045, and **jwst** package version 1.8.3 (28). As described
 381 in ref. (13; 27), we assume a constant gain of 3.1 electrons/DN (same as
 382 for the SPARTA reduction; see below), which is closer to the true gain
 383 than the value of 5.5 currently assumed in the CRDS reference files (private
 384 comm., Sarah Kendrew). **Eureka!**’s Stage 1 jump step’s rejection threshold
 385 was increased to 7.0 and Stage 2’s photom step was skipped (to more easily
 386 estimate the expected photon noise), but otherwise the Stage 1–2 processing
 387 was done following the **jwst** pipeline’s default settings. We also evaluated the
 388 use of an experimental non-linearity reference file developed to address MIRI’s
 389 “brighter-fatter effect”(29), but we ultimately decided to stick with the default
 390 non-linearity reference file as the final transmission spectra changed by less
 391 than 1σ at all wavelengths.

392 We extracted columns 11–61 and rows 140–393 as pixels outside of this
 393 range are excessively dominated by noise. We masked pixels marked as
 394 “DO_NOT_USE” in the DQ array to remove bad pixels identified by the **jwst**
 395 pipeline. To aid in decorrelating systematic noise, we compute a single cen-
 396 troid and PSF-width for each integration by summing along the dispersion
 397 direction and fitting a 1D Gaussian; only the first integration’s centroid was
 398 used to determine aperture locations. We subtracted the background flux by
 399 subtracting the mean of pixels separated from the source by 11 or more pixels

400 after first sigma-clipping 5σ outliers along the time axis and along the spatial
 401 axis. We then performed optimal spectral extraction (30) using the pixels
 402 within 5 pixels of the centroid. Our spatial profile was a cleaned median frame,
 403 following the same sigma-clipping methods described by ref. (13; 27). We then
 404 spectrally binned the data into 28 bins, each $0.25 \mu\text{m}$ wide, spanning $5\text{--}12 \mu\text{m}$
 405 as well as a single white light curve spanning the full $5\text{--}12 \mu\text{m}$. To remove
 406 any remaining cosmic rays or the effects of any high-gain antenna moves, we
 407 then sigma-clipped each light curve, removing any points 4 or more sigma
 408 discrepant with a smoothed version of the light curve computed using a box-
 409 car filter with a width of 20 integrations. This removed errant points while
 410 ensuring not to clip the transit ingress or egress.

411 When fitting, our astrophysical model consisted of a `starry` (31) transit
 412 model with uninformative priors on the planet-to-star radius ratio and uncon-
 413 strained, reparameterized quadratic limb-darkening parameters (32). We also
 414 used broad priors on the planet’s orbital parameters to verify that these new
 415 data are consistent with the orbital solution presented by ref.(33). Specifically,
 416 we used Gaussian priors for the transit time, inclination, and scaled semi-major
 417 axis based on the values of ref.(33) which were derived by fitting all previous
 418 WASP-39b observational datasets at once, see values in Extended Data Table
 419 1, but with greatly inflated uncertainties (roughly $10\times$ or higher than the
 420 precision achievable with these MIRI data alone) to allow these data to inde-
 421 pendently verify the previously published values (33). We also assumed zero
 422 eccentricity and fixed the orbital period to the value of $4.0552842 \pm_{0.0000035}^{0.0}$
 423 days from ref.(33). We linearly decorrelated against the changing spatial pos-
 424 ition and PSF-width computed during Stage 3. We also allowed for a linear
 425 trend in time as well as a single weakly constrained exponential ramp to remove
 426 the well-known ramp at the beginning of MIRI/LRS observations (11; 13; 27).
 427 We also trimmed the first 10 integrations as they suffered from a particu-
 428 larly strong exponential ramp. There was no evidence for mirror tilts (35) in
 429 the observations nor any residual impacts from high-gain antenna moves after
 430 sigma-clipping the data in Stage 4. Finally, we also used a noise multiplier
 431 to capture any excess white noise and ensure a reduced chi-squared of 1. We
 432 then used PyMC3’s No U-Turns Sampler (36) to sample our posterior. We used
 433 two independent chains and used the Gelman–Rubin statistic (37) to ensure
 434 that our chains had converged ($\hat{R} < 1.01$), and then we combined the samples
 435 from the two chains and computed the 16th, 50th, and 84th percentiles of the
 436 1D marginal posteriors to estimate the best-fit value and uncertainty for each
 437 parameter.

438 As our determined orbital parameters were consistent with those deter-
 439 mined by ref.(33), we then fixed our orbital parameters to those of ref.(33) for
 440 our spectroscopic fits ensuring consistency with other JWST spectra for this
 441 planet. The limb-darkening parameters for our spectroscopic fits were given a
 442 Gaussian prior of ± 0.1 with respect to model-predicted limb-darkening coeffi-
 443 cient spectra (38; 39) based on the Stagger grid (40). We also evaluated more

444 conservatively trimming the first 120 integrations (instead of 10) for our spectroscopic fits, but found that the resulting spectra were changed by much less
 445 than 1σ at all wavelengths.

446 For our white light curve fit, we found a white noise level 26% larger than
 447 the estimated photon limit, while the spectroscopic channels were typically
 448 10–20% larger than the estimated photon limit. As our adopted gain of 3.1
 449 is only accurate to within $\sim 10\%$ of the true gain (which varies as a function
 450 of wavelength; private comm., Sarah Kendrew; (13; 27)), these comparisons
 451 to estimated photon limits only give general ideas of MIRI’s performance. An
 452 examination of our Allan variance plots (41) showed minimal red noise in our
 453 residuals. Our decorrelation against the spatial position and PSF-width showed
 454 that the shortest wavelengths were most strongly affected by changes in spatial
 455 position and PSF-width, with both driving noise at the level of ~ 100 ppm in
 456 the shortest wavelength bin; meanwhile, the impact at longer wavelengths was
 457 weaker and not as well constrained. The orbital parameters determined from
 458 the white light curve fit are summarized in Extended Data Table 1.

460 Tiberius

461 **Tiberius** is a pipeline to perform spectral extraction and light-curve fitting,
 462 which is derived from the LRG-BEASTS pipeline (42–44). It has been used in
 463 the analysis of JWST data from the ERS Transiting Exoplanet Community
 464 program and GO programs (2; 3; 45; 48).

465 In our reduction with **Tiberius**, we first ran STScI’s `jwst` pipeline on
 466 the `uncal.fits` files. We performed the following steps in the `jwst` pipeline:
 467 `group_scale`, `dq_init`, `saturation`, `reset`, `linearity`, `dark_current`,
 468 `refpix`, `ramp_fit`, `gain_scale`, `assign_wcs` and `extract_2d`. Our spectral
 469 extraction was run on the `gainscalestep.fits` files and we used the
 470 `extract2d.fits` files for our wavelength calibration. As explained in the `jwst`
 471 documentation, the `gain_scale` step is actually benign if the default gain set-
 472 ting is used. For that reason, the **Tiberius** reduction used units of DN/s.
 473 Ultimately, since we normalize our light curves and rescale the photometric
 474 uncertainties during light curve fitting, the units of the extracted stellar flux
 475 do not impact the transmission spectrum.

476 We did not perform the `jump` or `flat_field` steps. Instead of the jump step,
 477 we performed outlier detection for every pixel in the time-series by locating
 478 integrations for which a pixel deviated by $> 5\sigma$ from the median value for that
 479 pixel. Any outlying pixels in the time-series were replaced by the median value
 480 for that pixel. Next we performed spectral extraction. We first interpolated
 481 the spatial dimension of the data onto a new grid with $10\times$ the resolution,
 482 which improves flux extraction at the sub-pixel level. The spectra were then
 483 traced using Gaussians fitted to every pixel row from row 171 to 394. The
 484 means of these Gaussians were then fitted with a fourth-order polynomial.
 485 We then performed standard aperture photometry at every pixel row after
 486 subtracting a linear polynomial fitted across two background regions on either
 487 side of the spectral trace. We experimented with the choice of aperture width

4 Mid-Infrared Spectrum of WASP-39b

and background width to minimize the noise in the white light curve. The result was a 8-pixel-wide aperture and two 10-pixel-wide background regions offset by 8 pixels from the extraction aperture.

Next we cross-correlated each integration's stellar spectrum with a reference spectrum to measure drifts in the dispersion direction. The reference spectrum was taken to be the 301st integration of the time-series, as we clipped the first 300 integrations (80 minutes) to remove the ramp seen in the transit light curve. The measured shifts had an RMS of 0.002 pixels in the dispersion direction and 0.036 in the spatial direction (as measured from the tracing step). Next we integrated our spectra in $25 \times 0.25 \mu\text{m}$ -wide bins from $5\text{--}11.25 \mu\text{m}$ to make our spectroscopic light curves.

We fitted our light curves with an analytic transit light curve, implemented in `batman` (49), multiplied by a time trend. For the white light curve, this time trend was a quadratic polynomial, as a linear trend was not sufficient. This differed to the other reductions that treated the systematics as exponential ramps with a linear trend. For the spectroscopic light curves, we divided each spectroscopic light curve by the best-fitting transit and systematics model from the white light curve fit. A quadratic trend was not necessary for the spectroscopic light curves, which we instead fit with a linear trend to account for residual chromatic trends not accounted for by the common mode correction.

In all light curve fits, we used Markov Chain Monte Carlo (MCMC) implemented via `emcee` (50). We set the number of walkers equal to $10 \times$ the number of free parameters and ran two sets of chains. The first set of chains was used to rescale the photometric uncertainties to give $\chi_{\nu}^2 = 1$ and the second set of chains was run with the rescaled uncertainties. In both cases, the chains were run until they were at least $50 \times$ the autocorrelation length for each parameter. This led to chains between 4000–10000 steps long.

Given the non-linear ramp at the beginning of the observations, we clipped the first 300 integrations. We found this clipping led to a consistent and more precise transmission spectrum. In tests without clipping any integrations, we found that a fifth order polynomial was needed to fit the ramp. We disfavoured this due to the extra free parameters. For the white light curve, our fitted parameters were the time of mid-transit (T_0), orbital inclination of the planet (i), semi-major axis scaled by the stellar radius (a/R_*), planet-to-star radius ratio (R_P/R_*), the three parameters defining the quadratic-in-time polynomial trend, and the quadratic limb darkening coefficients reparameterized following (32) ($q1$ and $q2$). For $q1$ and $q2$ we used Gaussian priors with means set by calculations from Stagger 3D stellar atmosphere models (38–40) and standard deviations of 0.1. The period was fixed to 4.0552842518 d as found from the global fit to the near-IR JWST datasets (33). Our best-fitting values for the system parameters are given in Table 1.

For our spectroscopic light curves, we fixed the system parameters (a/R_* , i , T_0) to the values from the global fit to the near-IR JWST datasets (33). The median RMS of the residuals from the white light and spectroscopic light curve fits were 573 and 3034 ppm, respectively.

533 **SPARTA**

534 The Simple Planetary Atmosphere Reduction Tool for Anyone (SPARTA) is
 535 an open-source code intended to be simple, fast, barebones, and utilitarian.
 536 SPARTA is fully independent and uses no code from the JWST pipeline or
 537 any other pipeline. It was initially written to reduce the MIRI phase curve
 538 of GJ 1214b, and is described in detail in that paper (51). SPARTA was also
 539 used to reduce the MIRI phase curve of WASP-43b, taken as part of the
 540 Early Release Science program (13; 27). Having learned many best practices
 541 from these previous reductions, we performed virtually no parameter optimiza-
 542 tion for the current WASP-39b reduction. Below, we briefly summarize the
 543 reduction steps, but we refer the reader to the previous two papers for more
 544 details.

545 In stage 1, SPARTA starts with the uncalibrated files and performs nonlin-
 546 earity correction, dark subtraction, up-the-ramp fitting, and flat correction, in
 547 that order. The up-the-ramp fit discards the first 5 groups and the last group,
 548 which are known to be anomalous, and optimally estimates the slope using the
 549 remaining groups by taking the differences between adjacent reads and com-
 550 puting the weighted average of the differences. The weights are calculated with
 551 a mathematical formula which gives the optimal estimate of the slope (51).

552 After stage 1, SPARTA computes the background by taking the average of
 553 columns 10–24 and 47–61 (inclusive, zero-indexed) of each row in each integra-
 554 tion. The background is then subtracted from the data. These two windows
 555 are equally sized and equidistant from the trace on either side, so any slope in
 556 the background is naturally subtracted out.

557 Next, we compute the position of the trace. We compute a template by
 558 taking the pixel-wise median of all integrations. For each integration, we shift
 559 the template (via bilinear interpolation) and scale the template (via multipli-
 560 cation by a scalar) until it matches the integration. The shifts that result in
 561 the lowest χ^2 are recorded.

562 The aforementioned template, along with the positions we find, are used for
 563 optimal extraction. We divide the template by the per-row sum (an estimate of
 564 the spectrum) to obtain a profile, and shift the profile in the spatial direction
 565 by the amount found in the previous step. The shifted profile is then used for
 566 optimal extraction, using the algorithm of (30). We apply this algorithm only
 567 to a 11-pixel-wide (full width) window centered on the trace, and iteratively
 568 reject $> 5\sigma$ outliers until convergence.

569 After optimal extraction, we gather all the spectra and the positions into
 570 one file. We reject outliers by creating a white light curve, detrending it with
 571 a median filter, and rejecting integrations $> 4\sigma$ away from 0. Sometimes, only
 572 certain wavelengths of an integration are bad, not the entire integration. We
 573 handle these by detrending the light curve at each wavelength, identifying 4σ
 574 outliers, and replacing them with the average of their neighbors on the time
 575 axis.

576 Finally, we fit the white light and spectroscopic light curves using `emcee`.
 577 The spectroscopic bins are exactly the same as for the Eureka! and Tiberius

reductions: $0.25 \mu\text{m}$ wide and ranging from $5.00\text{--}5.25 \mu\text{m}$ to $11.75\text{--}12.00 \mu\text{m}$. We trim the first 112 integrations (30 minutes), and reject $> 4\sigma$ outliers. In the white light fit, limb darkening parameters q_1 and q_2 are both free and given broad uniform priors. In the spectroscopic fit, T_0 , P , a/R_s , b , and the limb darkening coefficients are fixed to the fiducial values, but the transit depth and the systematics parameters are free. The systematics model is given by

$$S = F_* (1 + A \exp(-t/\tau) + c_y y + c_x x + m(t - \bar{t})), \quad (1)$$

where F_* is a normalization constant, A and τ parameterize the exponential ramp, t is the time since the beginning of the observations (after trimming), x and y are the positions of the trace on the detector, m is a slope (potentially caused by stellar variability and/or instrumental drift), and \bar{t} is the average time. All parameters are given uniform priors. τ is required to be between 0 and 0.1, but no explicit bounds are imposed on the other parameters.

Forward Modelling

We used several forward models that take into account photochemistry to infer the properties of WASP-39b's atmosphere from the observations. These models are based on known first-principle physics and chemistry that aid in our understanding of the important atmospheric processes at work. In addition, we also use one of the models to generate a more extensive model grid to assess the atmospheric metallicity and elemental ratios of WASP-39b. These models compute the atmospheric composition by explicitly treating the thermochemical and photochemical reactions and transport in the atmosphere, and in general are initialized from equilibrium abundances based on a given elemental ratio, for which we scale relative to Solar abundances (52). Although the abundances of a planet's host star are the more natural comparison point (e.g., 53), the measured multi-element abundances of WASP-39 are very nearly Solar (54). All photochemical models use the same incident stellar spectrum as that described in ref. (4). Finally, we also consider a radiative-convective thermochemical equilibrium model that includes an injected SO_2 abundance and clouds to connect our work to previous interpretations of near-infrared JWST spectra of WASP-39b (2; 3; 15; 16).

VULCAN

The 1D kinetics model VULCAN treats thermochemical (58) and photochemical (8) reactions. VULCAN solves the Eulerian continuity equations including chemical sources/sinks, diffusion and advection transport, and condensation. We used the C–H–N–O–S network (https://github.com/exoclime/VULCAN/blob/master/thermo/SNCHO_photo_network.txt) for reduced atmospheres containing 89 neutral C-, H-, O-, N-, and S-bearing species and 1028 total thermochemical reactions (i.e., 514 forward-backward pairs) and 60 photolysis reactions. The sulphur allotropes are simplified into a system of S , S_2 , S_3 ,

S₄, and S₈. The sulphur kinetics data is drawn from the NIST and KIDA databases, as well as modelling (6; 60) and ab-initio calculations published in the literature (e.g., 62). The temperature-dependent UV cross sections (8) are not used in this work for simplicity, but preliminary tests show that their exclusion has resulted in only minor differences (less than 50% of the SO₂ VMR). Apart from varying elemental abundances, we applied an identical setup of VULCAN as that in ref. (4).

KINETICS

The KINETICS 1D thermo-photochemical transport model (63–66) is used to solve the coupled Eulerian continuity equations for the production, loss, and vertical diffusive transport of atmospheric species. The chemical reaction list, background atmospheric structure, and assumed planetary parameters are identical to those described in ref. (4), except here we explore additional atmospheric metallicities. Briefly, the C-H-N-O-S-Cl network used for the WASP-39b KINETICS model contains 150 neutral species that interact with each other through 2350 total reactions, with the non-photolysis reactions being reversed through the thermodynamic principle of microscopic reversibility (67).

ARGO

The 1D thermochemical and photochemical kinetics code, ARGO, originally utilised the Stand2019 network for neutral hydrogen, carbon, nitrogen and oxygen chemistry (68; 69). ARGO solves the coupled 1D continuity equation including thermochemical-photochemical reactions and vertical transport. The Stand2019 network was expanded by ref. (70) by updating several reactions, incorporating the sulphur network developed by ref. (7), and supplementing it with reactions from ref. (72) and ref. (73), to produce the Stand2020 network. The Stand2020 network includes 2901 reversible reactions and 537 irreversible reactions, involving 480 species composed of H, C, N, O, S, Cl and other elements.

EPACRIS

EPACRIS (ExoPlanet Atmospheric Chemistry & Radiative Interaction Simulator) is a general-purpose one-dimensional atmospheric simulator for exoplanets. EPACRIS has a root of the atmospheric chemistry model developed by Renyu Hu and Sara Seager at MIT (74–76), and since then has been reprogrammed and upgraded substantially (77; 78, and also Yang & Hu 2023, in prep. mainly focusing on the validation of reaction rate-coefficients). We use the atmospheric chemistry module of EPACRIS to compute the steady-state chemical composition of WASP-39 b's atmosphere controlled by thermochemical equilibrium, vertical transport, and photochemical processes. The chemical network applied in this study includes 60 neutral C-, H-, O-, and S-bearing

species and 427 total reactions (i.e., 380 reversible reaction pairs and 47 photodissociation reactions). In this chemical model, SO_2 volume mixing ratio is sensitive to two reactions which are (i) $\text{H}_2\text{S} \leftrightarrow \text{HS} + \text{H}$ and (ii) $\text{SO} + \text{OH} \leftrightarrow \text{HOSO}$). Briefly describing, if $\text{HS} + \text{H} \rightarrow \text{H}_2\text{S}$ recombination rate-coefficient is faster than $10^{-11} \text{ cm}^3/\text{molecule/s}$ (collision-limit is around $10^{-9} \text{ cm}^3/\text{molecule/s}$), this will result in inefficient H_2S dissociation (i.e., H_2S starts to dissociate at higher altitude), which leads to the decreased SO_2 formation. Unfortunately, to the best of our knowledge, there is no theoretically calculated nor experimentally measured H_2S decomposition rate coefficient. For this reason, in EPACRIS, we assumed that $\text{H}_2\text{S} \leftrightarrow \text{HS} + \text{S}$ is similar to $\text{H}_2\text{O} \leftrightarrow \text{HO} + \text{H}$. However, all the $\text{HS} + \text{H} \rightarrow \text{H}_2\text{S}$ recombination rate-coefficient used in different models were slower than $10^{-11} \text{ cm}^3/\text{molecule/s}$ and below this range, SO_2 volume mixing ratio isn't sensitive to this reaction anymore. With regard to the $\text{SO} + \text{OH} \leftrightarrow \text{HOSO}$ reaction, the forward reaction (barrier-less reaction) is favored at lower temperatures and higher pressure according to the HOSO potential energy surfaces (79). For this reason, the exclusion of this reaction from the EPACRIS chemical model shows up to 2 orders of magnitude increase (i.e., from $[\text{SO}_2] \sim 10^{-6}$ to 10^{-4}) in the SO_2 volume mixing ratio in the morning limb. However, in the evening limb whose temperature is up to ~ 200 K higher compared to the morning limb, HOSO now can further dissociate to form SO_2 and H due to elevated temperature, which results in the increased $[\text{SO}_2] \sim 10^{-5}$ compared to the morning limb $[\text{SO}_2] \sim 10^{-6}$.

679 IDIC Grid

680 Ref. (14) presented a grid of VULCAN photochemistry models (we term this the
681 **IDIC** grid) for WASP-39b that cover a 3D volume of possible C, O, and S
682 elemental abundances without aerosols. We used these models to compare to
683 our three spectral reductions. We fit each MIRI/LRS transmission spectrum
684 by binning all model spectra to the regular, $0.25 \mu\text{m}$ resolution of the observed
685 spectra, allowing for an arbitrary vertical offset for each model spectrum, and
686 calculating χ^2 for each model spectrum. We first determined the goodness-of-fit
687 while holding all abundances linked to the same value (i.e., C, O, and S all
688 enhanced by the same level relative to Solar abundances). We fit a parabola
689 to the three lowest χ^2 points to estimate the optimal elemental abundance
690 enhancement and its uncertainty (i.e., where $\Delta\chi^2 = 1$; 81). We then also com-
691 pared these linked-abundance χ^2 values to those derived across the entire 3D
692 grid by allowing all three elemental abundances to vary individually. Extended
693 Data Tables 2 and 3 show the abundances and χ^2 values for these analyses.

694 Interpreting the spectra is challenging because the goodness-of-fit varies
695 widely across the observed spectra: across all IDIC models, we find a best-fit χ^2
696 of 14.7 for the Tiberius reduction but a best-fit $\chi^2 = 45.4$ for the Eureka! reduc-
697 tion (which reports much smaller measurement uncertainties). Nonetheless the
698 linked analyses all suggest a bulk metallicity of $7.1\text{--}8.0 \times$ Solar. The standard
699 deviation of the optimal metallicity values is 0.4, smaller than the average
700 uncertainties in Extended Data Table 2, suggesting that the uncertainty in the

701 bulk metallicity is dominated by statistical (or model-dependent systematic)
 702 uncertainties rather than by differences between the several reduced spectra.

703 When allowing C, O, and S abundances to each vary freely, in all cases
 704 the best-fitting models show a preference for super-solar O/S ratios, sub-solar
 705 C/O, and approximately solar C/S ratios. Ref. (14) suggests that these ratios
 706 could be used to constrain a planet's formation history by comparing to forma-
 707 tion models (53; 82). However, a Bayesian Information Criterion (BIC) analysis
 708 shows that for the Tiberius and SPARTA reductions the observed spectra do
 709 not justify the additional free parameters of multiple independent elemental
 710 abundances. The formal BIC value for the Eureka! reduction seems to indicate
 711 that independent abundances are justified, but this conclusion seems ques-
 712 tionable since this spectrum gives the worst χ^2 values (36.7 with just 28 data
 713 points).

714 PICASO Grid

715 Previous observations of WASP-39b with JWST's NIRspec PRISM, NIRISS
 716 SOSS, NIRCam F322W, and NIRSpec G395H (1–3; 15; 16) were interpreted
 717 using a grid of 1D radiative-convective thermal equilibrium (RCTE) models
 718 (84) generated with PICASO 3.0 (85; 86). Here, to interpret the spectrum of
 719 WASP 39b observed with MIRI LRS, we use the base clear equilibrium PICASO
 720 3.0 version of this grid along with a subset of the grid of PICASO 3.0 models
 721 post-processed with Virga (87; 88) to account for clouds formed from Na₂S,
 722 MnS, and MgSiO₃. The full parameters of the original set of grids can be found
 723 in ref. (84). We reduced several gridpoints of the post-processed cloudy Virga
 724 grid. In the cloudy grid we use here, we included only one heat redistribution
 725 factor (0.5), only one intrinsic temperature (100 K), only f_{sed} values ≤ 3 ,
 726 and only $\log_{10} K_{zz} > 5$, as this low of a $\log_{10} K_{zz}$ is unphysically small at
 727 temperatures > 500 K (e.g., Fig. 2; 89), as in the atmosphere of WASP-39b.
 728 The original grids in ref. (84) were only computed for wavelengths from 0.3
 729 to 6 μm ; here we extend the simulated transmission spectra of the grid out to
 730 wavelengths of 15 μm .

731 To assess the presence of SO₂ in the MIRI LRS data, we first inject a
 732 constant abundance of SO₂ into each model at gridpoints of 3 ppm, 5 ppm,
 733 7.5 ppm, 10 ppm, 20 ppm, and 100 ppm, and we then recompute the model
 734 spectra. These values of SO₂ are therefore not chemically consistent with the
 735 rest of the atmosphere. As in the IDIC grid, we fit each transmission spectrum
 736 reduction by binning the model spectra (resampled to opacities at R=20,000
 737 (90)) to the resolution of the observations, allow for a vertical offset, and
 738 calculate χ^2 for each model spectrum. We take the top 20 best-fitting models
 739 to account for scatter in the preferred grid values and discard clear outliers.

740 Without SO₂, although we find comparable overall fits ($\chi^2 \leq 2.6$) to the
 741 data for the Eureka! reduction, none of the SO₂-free RCTE models capture
 742 the rise around 7.7 μm or 8.5 μm . Once SO₂ is added, we find that the overall
 743 model fit to the Eureka! reduction is slightly worse ($\chi^2 \leq 2.7$), but the shape
 744 of the spectrum better matches at 7.7 μm and 8.5 μm . This slightly worse fit

is driven by the slightly higher transit depths from $5 - 6 \mu\text{m}$ in the **Eureka!** reduction, which results in a higher baseline “continuum” when SO_2 is not included. For both the SPARTA and **Tiberius** reductions, the grid model fits improve with added SO_2 . Most crucially, in the absence of SO_2 , the best-fitting clear PICASO 3.0 and cloudy PICASO 3.0 + **Virga** grid models across all reductions are dominated by H_2O absorption, as well as prominent contributions from CH_4 for the **Tiberius** and **Eureka!** data, as shown in Extended Data Figure 3. For the **Tiberius** and **Eureka!** reductions, cloudy cases without SO_2 result in high inferred amounts of CH_4 ($\text{VMR} \sim 1-50 \text{ ppm}$) at 10 mbar—where the MIRI/LRS observations probe. These CH_4 mixing ratios are in disagreement with the lack of CH_4 in WASP-39b’s atmosphere observed at shorter wavelengths with NIRISS, NIRSpec, and NIRCam (with best-fit models having CH_4 VMRs of $\sim 3 \text{ ppb}$, $\sim 0.1 \text{ ppm}$, and $\sim 50 \text{ ppb}$, respectively) (2; 3; 15; 16). With the SPARTA reduction, rather than compensating for the lack of SO_2 opacity with elevated CH_4 abundances, the PICASO grid best-fits invoke opacity from a high altitude, optically thick silicate cloud.

Models with SO_2 injected produce better overall fits to each MIRI reduction, with mixing ratios of carbon, oxygen, and sulfur-bearing species in agreement with those inferred from shorter wavelength data from NIRISS, NIRSpec, and NIRCam. Therefore, our results suggest MIRI data alone can independently constrain relevant atmospheric gaseous species. With these MIRI data in addition to the previous JWST observations, we demonstrate that SO_2 in WASP-39b’s atmosphere is required to self-consistently interpret the data from JWST over a wide wavelength range.

When SO_2 is included in the RCTE PICASO 3.0 models, we find that all three reductions prefer C/O ratios of \leq Solar values. These low C/O ratios result from the lack of methane needed to fit the data. Metallicity values range from $\sim 10 \times$ Solar for the **Eureka!** and **Tiberius** reductions to $\sim 10-30 \times$ Solar for the SPARTA reduction. Best-fits are comparable between clear and cloudy cases, with high best-fitting values of f_{sed} resulting in cloud decks below the atmospheric regions probed by MIRI/LRS. The best-fitting models using MIRI therefore result in very different cloud parameters than models fit to shorter wavelengths (2; 3; 15; 16). These cloud parameter discrepancies highlight that constraining cloud conditions requires wide wavelength coverage and may result from cloud formation localized to different atmospheric layers (20).

Finally, within the framework of injected uniform SO_2 abundances that do not vary with altitude, we find that all of our SO_2 abundance grid points result in comparable model fits, preventing a strong SO_2 abundance constraint from the PICASO 3.0 grid.

Retrieval Modelling

In addition to forward modelling, we further investigated the atmosphere of WASP-39b as seen by MIRI/LRS using six different free-retrieval frameworks (see descriptions below). Free retrievals use parameterized atmospheric models

to directly extract constraints on atmospheric properties from the data. Each chemical species in the model is treated as an independent free parameter, rather than abundances being calculated under assumptions such as chemical equilibrium or photochemistry. The retrievals presented in this paper all assume that the atmosphere is well-mixed, so chemical abundances are held constant throughout the atmosphere. All retrievals also assume an isothermal temperature profile, since the MIRI-LRS spectrum probes a relatively small range of atmospheric pressures and therefore is relatively insensitive to the temperature structure. All retrievals contain some prescription for aerosols, but the details vary across the six frameworks and are described in more detail below. This variation in aerosol treatment is intentional, and by this approach we hope to capture the impact of different retrieval choices on molecular detection and abundance measurements for MIRI. All frameworks also retrieve either a reference pressure or reference radius, to account for the so-called ‘normalization degeneracy’ (see (91)). Helios-r2 also includes the stellar radius and $\log(g)$, where g is gravitational acceleration, as free parameters. For all frameworks, we ran the preferred model set up, and those removing H₂O or SO₂, allowing us to calculate their Bayesian evidence following (92) (Extended Data Table 4).

Atmospheric models do not provide as good a match to the data at $\gtrsim 10\mu\text{m}$, with worse fits by χ^2 and p-value metrics than when only considering data bluewards of $10\mu\text{m}$. Therefore, we considered the possibility of retrieving only on the short wavelengths. While we find that the retrieved abundances are highly sensitive to the wavelengths considered, there is no evident, data-driven argument to disregard data at longer wavelengths, and the fits are acceptable. Therefore, the atmospheric inferences presented below consider the entire MIRI-LRS spectrum from 5 to $12\mu\text{m}$. Further investigation into the apparent decrease in transit depth at $10\mu\text{m}$ is warranted in future work.

ARCiS

ARCiS (ARtful modelling Code for exoplanet Science) is an atmospheric modelling and Bayesian retrieval package (93; 94), which utilises the Multinest (95) Monte Carlo nested sampling algorithm to sample a parameter space for the region of maximum likelihood. ARCiS is capable of both free molecular and constrained chemistry (i.e. assuming thermochemical equilibrium) retrievals, with the latter using GGchem (96) for the chemistry. For this work we use a free molecular retrieval with a simple grey, patchy cloud model. This simple model parameterises cloud-top pressure and the degree of cloud coverage (from 0 for completely clear to 1 for completely covered). We explored the use of a variety of molecular species in our retrievals, with the majority of their abundances being unconstrained by the retrieval of this dataset. In particular, we searched for additional photochemical products including SO and SO₃. The photochemical model of ref. (4) predicts observable amounts of SO but very little SO₃. We find some weak-to-moderate (2.5σ) evidence for SO (97) and no

evidence of SO_3 (98), qualitatively matching the photochemical model predictions. In addition, we find $\sim 3.3\sigma$ evidence for the presence of a molecule such as SiH (99), BeH (100), or NO (101). The broad opacity features from these species, however, are indistinguishable from a continuum effect such as haze.

In the absence of other spectral features from these molecules, and because we do not expect SiH, BeH, or NO to be abundant enough (~ 1000 ppm are required, compared to a maximum of ~ 10 ppm for SiH and fractions of a ppm for BeH under the assumption of solar-abundance thermochemical equilibrium (52; 96)), we exclude them in our models. We therefore present a simplified set of molecules, with only H_2O (22) and SO_2 (23) included, along with the parameters for the clouds. Combined with isothermal temperature and planetary radius, this totals six free parameters. The reference pressure for the radius is 10 bar. The opacities are k-tables from the ExoMolOP database (104), with the linelists from the ExoMol (105) or HITEMP (106) database as specified. Collision-induced absorption for H_2 and He are taken from refs. (107) and (108). We use 1000 live points and a sampling efficiency of 0.3 in Multinest. We used a value of $0.281 M_J$ for the planetary mass, and $0.9324 R_\odot$ for the stellar radius.

Aurora

Aurora is an atmospheric inference framework with applications to transmission spectroscopy of transiting exoplanets (e.g., 109; 110). The comprehensive description of the framework and modelling paradigm are explained in ref. (111). For this dataset we considered a series of atmospheric models ranging from simple cloud-free isothermal models, to those with multiple chemical species, inhomogeneous cloud and hazes, and non-isothermal pressure-temperature (PT) profiles. The parameter estimation was performed using the nested sampling algorithm (112) through MultiNest (113) using the PyMultiNest implementation (114).

We find that the retrieved abundances of H_2O and SO_2 vary by several orders of magnitude depending on the data reduction considered, the wavelength range included (e.g., above or below $10 \mu\text{m}$), and assumptions about the atmospheric model used (e.g, cloud-free vs. cloudy, fully cloudy vs. inhomogeneous clouds, multiple absorbers vs. limited absorbers; see, e.g., 115).

Our initial exploration of atmospheric models finds that when considering multiple species (e.g., Na, K, CH_4 , NH_3 , HCN, CO, CO_2 , C_2H_2), their abundances are largely unconstrained despite affecting the retrieved SO_2 abundances by at least an order of magnitude, generally skewing them towards lower values (e.g., $\log_{10}(\text{SO}_2) \lesssim -6$). The use of parametric PT profiles (e.g., 116) do not result in significant changes to the retrieved abundances and the resulting temperature profiles are largely consistent with isothermal atmospheres. Finally, we find that assuming cloud-free or homogeneous cloud cover can result in artificially tight constraints on the H_2O abundances as expected (e.g., 111; 115; 117), motivating our choice to consider the presence of inhomogeneous clouds/hazes.

Given the above considerations, we settled on a simplified fiducial model to calculate the model preference (i.e., ‘detection’; see, e.g., 111; 118) for H₂O and SO₂ with the caveat that the retrieved abundances are highly dependent on the model/data assumptions. This simplified model only considers absorption due to H₂O and SO₂ using line lists from (106) and (23) respectively, H₂–H₂ and H₂–He collision-induced absorption with line lists from (119), the presence of inhomogeneous clouds and hazes following the single sector model in ref. (111) (see also 117; 120), and an isothermal pressure temperature profile. In total, our atmospheric model has eight free parameters: two for the constant-with-height volume mixing ratios of the chemical species considered, one for the isothermal temperature of the atmosphere, four for the inhomogeneous clouds and hazes, and one for the reference pressure for the assumed planet radius ($R_p = 1.279 R_J$, $\log_{10}(g) = 2.63$ cgs, $R_{\text{star}} = 0.932 R_\odot$). The forward models for the parameter estimation were calculated at a constant resolution $R= 10,000$ using 1000 live points for MultiNest.

CHIMERA

CHIMERA (121) is an open-source radiative transfer and retrieval framework which has been extensively used to study the atmospheres of planetary mass objects, ranging from brown dwarfs (122) to terrestrial planets (123). The forward model is coupled to a nested sampler, namely MultiNest (95) using the PyMultiNest (114) wrapper. CHIMERA takes advantage of the correlated-k approximation (124; 125) in order to rapidly compute the transmission through the atmosphere. Given the flexible nature of the code, it is capable of modelling a range of different aerosol and cloud scenarios (126), as well as a range of different thermal structures (116; 127).

For this work we are limited to the spectral bands we have access to, thus, we only model H₂O and SO₂ using line data from refs. (22) and (23) respectively. We assume the atmosphere is dominated by H₂, with a He/H₂ ratio of 0.1764; therefore, we also model the H₂–H₂ and H₂–He collision-induced absorption (119). We model hazes following the prescription of (128), which treats hazes as enhanced H₂ Rayleigh scattering with a free power-law slope. Alongside the haze calculation, we fit for a constant-in-wavelength grey cloud with opacity κ_{cloud} . We also assess the patchiness of the cloud by linearly combining a cloud-free model with the cloudy model (129). We find that the inclusion of hazes does not improve any of our inferences, thus our final model presented is from using the grey cloud alone. We used a value of $0.281 M_J$ for the planetary mass, and $0.932 R_\odot$ for the stellar radius.

Helios-r2

Helios-r2 (The open-source Helios-r2 code can be found here: <https://github.com/exoclime/Helios-r2>) (130) is an open-source, GPU-accelerated retrieval code for atmospheres of exoplanets and brown dwarfs and can be used for transmission, emission, and secondary-eclipse observations (see, e.g., (131), (132), or (133)). It uses a Bayesian nested sampling approach to compute the

919 posterior distributions and Bayesian evidences, based on the `MultiNest` library
 920 ([95](#)).

921 In `Helios-r2` the chemical composition can be constrained assuming
 922 chemical equilibrium using the `FastChem` (The open-source `FastChem` code
 923 can be found here: <https://github.com/exoclime/FastChem>) chemistry code
 924 ([134](#); [135](#)) or by performing a free abundance retrieval with either isoprofiles
 925 or vertically varying abundances. The temperature profile can also be either
 926 described by an isoprofile or allowed to vary with height by using a flexi-
 927 ble description based on piece-wise polynomials or a cubic spline approach.
 928 Given the limited number of available observational data points in this study,
 929 we chose to describe the temperature and the chemical abundances with
 930 isoprofiles.

931 In our final retrieval calculations only two gas-phase species are directly
 932 retrieved (H_2O and SO_2), while H_2 and He are assumed to form the background
 933 atmosphere based on their solar H/He ratio. Additional chemical species,
 934 such as HCN , CO , CO_2 , or CH_4 for example, were tested but resulted in
 935 unconstrained posteriors.

936 We used the Exomol POKAZATEL line list for H_2O ([22](#)) and the ExoAmes
 937 SO_2 ([23](#)) line list in our retrievals. Line list data for HCN , CO , and CH_4 were
 938 taken from ([136](#)), ([137](#)), and ([138](#)) respectively. The opacities were calculated
 939 with the open-source opacity calculator HELIOS-K (The open-source HELIOS-K
 940 code can be found here: <https://github.com/exoclime/HELIOS-K>) ([139](#); [140](#))
 941 and are available on the DACE platform (<https://dace.unige.ch>). The collision-
 942 induced absorption of H_2-H_2 and H_2-He pairs was taken from ([141](#)), ([142](#)),
 943 and ([143](#)).

944 In the retrieval calculations, we added a grey cloud layer with the cloud's
 945 top pressure as a free parameter. Additionally, we used the surface gravity
 946 and the stellar radius as free parameters with Gaussian priors based on their
 947 measured values to incorporate their uncertainties in the retrieval results.

948 For the retrieval calculations in this study, 2000 live points and a sampling
 949 efficiency of 0.3 for an accurate determination of the Bayesian evidence were
 950 used.

951 NEMESIS

952 NEMESIS ([144](#)) is an open-source retrieval algorithm that allows simulation of
 953 a range of planetary and substellar bodies, using either nested sampling ([112](#);
 954 [145](#)) or optimal estimation ([146](#)) to iterate towards a solution. It has been used
 955 extensively to model the atmospheres of transiting exoplanets (e.g., ([117](#))).
 956 NEMESIS uses the correlated-k approximation ([124](#)) to allow rapid calculation
 957 of the forward model. It allows flexible parameterization of aerosols and gas
 958 abundance profiles, and can also be used to simultaneously and consistently
 959 model multiple planetary phases (e.g., ([147](#))).

960 In this work, we use the nested sampling algorithm PyMultiNest ([95](#); [114](#)),
 961 with 2000 live points. We include H_2O line data from the POKAZATEL linelist

(22) and SO₂ line data from the ExoAmes linelist (23), using k-tables calculated as in (104). Collision-induced absorption information for H₂ and He is taken from (107) and (108). Aerosol is modelled as an opaque grey cloud deck, with a variable top pressure. We also retrieve a fractional cloud coverage parameter, simulating the total terminator spectrum as a linear combination of a cloudy spectrum and an otherwise identical clear spectrum. We also tested the inclusion of a simple haze model with a tunable scattering index parameter, after refs. (120) and (117), but found that the retrieved scattering index gave an unrealistically steep spectral slope. We therefore present the models including only a grey cloud deck. We used a value of 0.281 M_J for the planetary mass, and 0.9324 R_\odot for the stellar radius.

PyratBay

PYRATBAY(24), PYthon RAdiative-Transfer in a BAYesian framework, is an open-source software that enables atmospheric forward and retrieval modelling of exoplanetary spectra (148). This software utilizes parametric temperature, composition, and altitude profiles as a function of pressure to generate emission and transmission spectra. The radiative transfer module considers various sources of opacity, including alkali lines (149), Rayleigh scattering (150; 151), Exomol and HITEMP molecular line lists (106; 152), collision-induced absorption (107; 108), and cloud opacities. To optimize retrieval, PYRATBAY compresses these large databases while retaining essential information from dominant line transitions, using the method described in ref. (153). The software offers various cloud condensate prescriptions, including the classic “power law+gray” model, a “single-particle-size” haze profile, a “patchy clouds” model with partial coverage factor (154), and a complex parameterized Mie-scattering thermal stability model (155–157). Furthermore, PYRATBAY allows users to adjust the complexity of the compositional model, ranging from a “free retrieval” approach where molecular abundances are freely parameterized to a “chemically consistent” retrieval that assumes chemical equilibrium. For the chemically consistent retrieval, users can choose between the numerical TEA code (158; 159) and the analytical RATE code (160), both of which can rapidly calculate volume mixing ratios of desired elemental and molecular abundances across a wide range of chemical species. The software also provides a variety of temperature models, including isothermal profiles and physically motivated parameterized models (e.g., 116; 127). To sample the parameter space and perform Bayesian inference, PYRATBAY is equipped with two Bayesian samplers: the differential-evolution Markov Chain Monte Carlo (MCMC) algorithm (161), implemented via ref. (162), and the nested-sampling algorithm, implemented via PyMultiNest (113; 163). These algorithms utilize millions of models and thousands of live points to explore the parameter space effectively.

For this analysis, we conducted a free retrieval and tested various model assumptions. These involved testing all temperature parametrizations implemented in our modelling framework, a wide range of chemical species opacities

expected to exhibit observable spectral features in the MIRI wavelength region, H₂O (22), CH₄ (164), NH₃ (165; 166), HCN (136; 167), CO (137), CO₂ (168), C₂H₂ (169), SO₂ (23), H₂S (170), and different cloud prescriptions. Our transmission spectrum was generated at a resolution of R~15000 and then convolved to match the MIRI resolution of 100. We assumed a hydrogen-dominated atmosphere with a He/H₂ ratio of 0.1764 and accounted for H₂-H₂ (171) and H₂-He (171) collision-induced absorptions. We used the same values of the stellar radius and planetary mass as the NEMESIS pipeline. To evaluate the likelihood of our models, we utilized the PyMultiNest algorithm with 2000 live points. Similar to the findings of other retrieval frameworks, the majority of the considered species were largely unconstrained. The Mie-scattering cloud models did not detect spectral signatures of any condensates in the data, and the more complex temperature models yielded temperature profiles that were largely consistent with an isothermal atmosphere. Only H₂O and SO₂ exhibited detectable spectral features in the data, and the assumption of a patchy gray cloud was the most suitable for the quality of the observations. Our final atmospheric model, applied to each team's reduction data, consisted of six free parameters: two for the constant-with-height volume mixing ratios of the chemical species, one for the isothermal temperature of the atmosphere, one for the planetary radius, and two for the patchy opaque cloud deck.

1026 TauREx

1027 TauREx, Tau Retrieval for Exoplanets, is an open-source fully Bayesian inverse
 1028 atmospheric retrieval framework (172; 173). We adopted the latest version
 1029 (3.1) of the TauREx software (174; 175). This version makes exclusive use
 1030 of absorption cross sections, as the correlated- k tables are no longer com-
 1031 putationally advantageous (174). We selected the PyMultinest algorithm to
 1032 sample the parameter space (95; 114). The atmosphere was modeled with 200
 1033 equally spaced layers in log-pressure between 10⁶ and 10⁻⁴ Pa. In all our tests,
 1034 we assumed an isothermal profile and constant mixing ratios with altitude.
 1035 The radiative transfer model accounts for absorption from chemical species,
 1036 collision-induced absorption by H₂-H₂ and H₂-He (141–143), and clouds. We
 1037 performed initial retrieval tests including a long list of molecular species, H₂O
 1038 (22), SO₂ (23), CO (137), CO₂ (168), CH₄ (138), HCN (176), NH₃ (177), FeH
 1039 (178) and H₂S (170), but found that only H₂O and SO₂ may have detectable
 1040 features in the observed MIRI spectra. We validated statistically the detection
 1041 of both H₂O and SO₂ by comparing the Bayesian evidence of best-fit retrievals
 1042 with both species versus those obtained by removing either molecule. We con-
 1043 sidered the following scenarios: (1) a clear atmosphere, (2) an atmosphere with
 1044 an optically-thick cloud deck, for which we fitted the top-layer pressure, and
 1045 (3) an atmosphere with haze, using the formalism of ref. (179) for modelling
 1046 the Mie scattering. We finally selected the retrievals with a thick cloud deck,
 1047 which provide the most consistent scenarios across data reductions, and with
 1048 slightly more conservative error bars. Only for the Eureka! reduction, the

1049 haze model was slightly favored (2.4σ), but the corresponding molecular abundances
 1050 are affected by strong degeneracy between water and haze. For other reductions,
 1051 the inferred molecular abundances are essentially independent of the retrieval scenario.
 1052 We used a value of $0.281 M_J$ for the planetary mass, and $0.939 R_\odot$ for the stellar radius.
 1053

1054 Free retrieval results

1055 The results from all retrieval frameworks, across all three reductions, are presented
 1056 in Extended Data Table 4 and shown in Extended Data Figure 4. These serve to illustrate
 1057 the general consistency of the results for SO_2 and H_2O , whilst also highlighting the differences in retrieved abundance for some cases.
 1058 We reiterate that the different retrieval teams made a variety of choices in the setup
 1059 of their retrievals, which are described in more detail above. The overall good agreement
 1060 is testament to the robustness of our detection of SO_2 in the MIRI dataset.
 1061

1062 We recover a range of median abundances for $\log(\text{SO}_2)$ between -5.9 and -5.0 across all reductions and retrieval frameworks. The overall spread of $\log(\text{SO}_2)$ across all retrievals and reductions, from the lowest -1σ bound to the highest $+1\sigma$ bound, is -6.4 — -4.6 (the range reported in the main text refers only to the retrievals on the **Eureka!** reduction), corresponding to volume mixing ratios of 0.4 — 25 ppm (0.5 — 25 ppm if only retrievals on the **Eureka!** reduction are considered). Note that this range could potentially be wider if a more extensive exploration of possible cloud and haze configurations were conducted, which we leave to future work.

1063 SO_2 is detected at more than 3σ significance in all cases except the Helios-
 1064 r2 retrievals for **Eureka!** and SPARTA (2.54σ and 2.99σ respectively), and the Aurora retrieval for SPARTA (2.95σ). The Helios-r2 model has the simplest representation of clouds, but also allows the stellar radius and planetary
 1065 $\log(g)$ to vary, so it is likely that the precise combinations of the **Eureka!** and SPARTA spectra and the chosen variables result in weaker detections for SO_2 , because other parameters have more freedom to compensate for a lack of SO_2
 1066 in this framework. Similarly, the Aurora framework has a unique representation of aerosol, including both cloud and haze, with the cloud top pressure as a free parameter. This also increases the flexibility of the model to compensate for changes in the SO_2 abundance. In summary, free retrievals provide a broadly consistent picture, which is also consistent with the SO_2 volume mixing ratios from the best-fitting photochemical models (see e.g. Figure 4).

1067 Test runs with the ARCiS retrieval also included SO opacity, which was not included in the other retrieval schemes. The existence of SO is not ruled out by these retrievals, with weak-to-moderate (2.5σ) evidence for it being present in the atmosphere. If present, it contributes to the spectrum at around $9 \mu\text{m}$ and is an additional source of opacity overlapping with the longer wavelength end of the broad SO_2 feature. The presence of SO is consistent with photochemical predictions, and should be an avenue for future exploration.

We also retrieve $\log(\text{H}_2\text{O})$ abundances in all cases. For the most part, the median values for nearly all retrievals and reductions range from $\log(\text{H}_2\text{O})$ of -2.3 to -1.1, with an anomalously low value for the **Eureka!** reduction and the Aurora (-3.9) retrieval. This retrieval framework includes haze, so we postulate that in this case the haze slope is compensating for the shape of the H_2O feature. Whilst the CHIMERA retrieval also includes haze and cloud, the cloud is uniformly distributed and the opacity is scaled, whereas Aurora has the cloud top pressure as a free parameter. This likely accounts for the different solutions between these two codes. The **Eureka!** reduction also results in a spectrum with a slightly smoother downward slope between 5.2 and 6.5 μm than the other two reductions, which contributes to the preference for haze over H_2O absorption in the Aurora retrieval.

The main H_2O absorption feature in the MIRI-LRS range is a broad feature centered around 6 μm , but extending beyond the short wavelength cut off and also into the region affected by SO_2 . Slight differences in the shape of the spectrum between the three reductions at the shortest wavelengths, which is the region most sensitive to H_2O , drive the subtle differences in the retrieved H_2O abundances between those reductions. **Eureka!** and SPARTA have very similar transit depths and yield slightly larger H_2O abundances (range excepting outliers: -1.9 to -1.1) than the Tiberius reduction (range: -2.3 to -1.5).

Whilst all retrievals include some prescription for cloud and/or haze, the parameters are generally poorly constrained. For ARCS, CHIMERA and PyratBay, no meaningful constraints on any cloud properties were obtained for any reductions. For Helios-r2, 1 σ lower limits on $\log(\text{cloud top pressure})$ in bar of -1.85, -1.62, and -1.78 are found for the **Eureka!**, Tiberius, and SPARTA reductions respectively. Similarly, TauREx provides 1 σ lower limits on $\log(\text{cloud top pressure})$ of -1.60, -1.97 and -2.03 for **Eureka!**, Tiberius and SPARTA. For NEMESIS, we find that the cloud top pressure and cloud fraction are degenerate, but high cloud fractions with low cloud top pressures are not permitted, so we can rule out high, opaque cloud covering a large percentage of the terminator. For Aurora/**Eureka!**, the haze scattering slope is constrained to $\gamma = -4.6^{+1.0}_{-1.8}$, consistent with a Rayleigh-scattering slope ($\gamma = -4$) within 1- σ . In summary, we can rule out a grey cloud extending to low pressures with broad terminator coverage, but otherwise with such varied results across reductions and retrievals we cannot place any constraints on cloud or haze properties.

Data Availability. The data used in this paper are associated with JWST program DD-2783 and are available from the Mikulski Archive for Space Telescopes (<https://mast.stsci.edu>). The data products required to generate Figs. 1-4 and Extended Data Figs. 1-5 are available here: <https://doi.org/10.5281/zenodo.10055845>. All additional data are available upon request.

Code Availability.

The codes VULCAN and gCMCRT used in this work to simulate composition and produce synthetic spectra are publicly available:

1137 VULCAN^(8; 58) (<https://github.com/exoclime/VULCAN>)
 1138 gCMCRT⁽¹⁸⁰⁾ (<https://github.com/ELeeAstro/gCMCRT>)
 1139 The SPARTA software to reduce JWST MIRI and NIRCam time-series spectra
 1140 is publicly available: SPARTA⁽⁵¹⁾ (<https://github.com/ideasrule/sparta>). The
 1141 Tiberius software to reduce and analyse JWST time-series spectra is publicly
 1142 available: Tiberius^(42; 44) (<https://github.com/JamesKirk11/Tiberius>). Six
 1143 of the free retrieval codes are available at the following locations: ARCiS
 1144 (<https://github.com/michielmin/ARCiS>); CHIMERA
 1145 (<https://github.com/mrline/CHIMERA>); Helios-r2
 1146 (<https://github.com/exoclime/Helios-r2>); NEMESIS
 1147 (<https://github.com/nemesiscode/radtrancode>); PyratBay
 1148 (<https://github.com/pcubillos/pyratbay>); TauREx
 1149 (https://github.com/ucl-exoplanets/TauREx3_public).

1150 The Eureka! analyses used the following publicly available codes to
 1151 process, extract, reduce and analyse the data: STScI's JWST Calibration
 1152 pipeline (28), Eureka! (25), starry (31), PyMC3 (36), and the standard
 1153 Python libraries numpy (181), astropy (182; 183), and matplotlib (184).

1154 **Acknowledgments.** This work is based on observations made with the
 1155 NASA/ESA/CSA JWST. The data were obtained from the Mikulski Archive
 1156 for Space Telescopes at the Space Telescope Science Institute, which is oper-
 1157 ated by the Association of Universities for Research in Astronomy, Inc., under
 1158 NASA contract no. NAS 5-03127 for JWST. These observations are associated
 1159 with program no. JWST-DD-2783, support for which was provided by NASA
 1160 through a grant from the Space Telescope Science Institute. T.B. acknowl-
 1161 edges funding support from the NASA Next Generation Space Telescope
 1162 Flight Investigations program (now JWST) via WBS 411672.07.05.05.03.02.
 1163 J.K.B. is supported by a UKRI/STFC Ernest Rutherford Fellowship (grant
 1164 ST/T004479/1). J.T is supported by the Eric and Wendy Schmidt AI in Sci-
 1165 ence Postdoctoral Fellowship, a Schmidt Futures program. J.B. acknowledges
 1166 the support received in part from the NYUAD IT High Performance Comput-
 1167 ing resources, services, and staff expertise. G.M. has received funding from the
 1168 European Union's Horizon 2020 research and innovation programme under the
 1169 Marie Skłodowska-Curie grant agreement No. 895525, and from the Ariel Post-
 1170 doctoral Fellowship program of the Swedish National Space Agency (SNSA).
 1171 B.-O. D. acknowledges support from the Swiss State Secretariat for Educa-
 1172 tion, Research and Innovation (SERI) under contract number MB22.00046.
 1173 E.A.M. acknowledges support from the Centre for Space and Habitability
 1174 (CSH) and the NCCR PlanetS supported by the Swiss National Science Foun-
 1175 dation under grants 51NF40_182901 and 51NF40_205606. We thank M. Marley
 1176 for constructive comments.

1177 **Author Contribution.** All authors played a significant role in one or more
 1178 of the following: development of the original ERS proposal, development of the
 1179 DDT proposal, preparatory work, management of the project, definition of the
 1180 observation plan, analysis of the data, theoretical modelling, and preparation
 1181 of this paper. Some specific contributions are listed as follows: D.P., E.K.H.L.,

J.L.B., P.G., S.-M.T., V.P., X.Z., J.K.B., J.T., J.K., M.L.-M., and K.B.S. made significant contributions to the design of the program. D.P., A.D.F., and P.G. provided overall program leadership and management. T.B., J.K., and M.Z. reduced the data, modelled the light curves, produced the planetary spectrum, and compared the different data analyses. J.T. and J.K.B. provided free retrieval analyses and also led the free retrieval efforts. S.-M.T. provided a forward model fit to the data and also led the forward modeling efforts. J.B., K.L.C., D.K., G.M., and L.W. provided free retrieval analyses. S.E.M. and I.J.M.C. contributed extensive forward model grids for constraining atmospheric metallicity and elemental ratios. S.J., J.I.M., and J.Y. contributed forward models, which were post-processed into spectra by E.K.H.L.. E.-M.A., A.B.-A., J.B., N.C., B.-O.D., K.D.J., E.A.M., A.D., R.H., P.-O.L., and J.I. contributed additional data reductions that are not shown in this paper, but provided valuable context for the highlighted reductions that was summarized by T.B.. S.L.C., L.F., M.L.-M., A.A.A.P., B.V.R., M.R., and S.R. served on the red team review of the paper, with J.L.B., R.H., and X.Z. offering additional vital comments. A.D.F., J.T., and S.E.M. generated the figures for this paper. D.P., A.D.F., P.G., J.K.B., T.B., J.K., M.Z., S.-M.T., S.E.M., and I.J.M.C. made significant contributions to the writing of this paper. J.T., J.B., K.L.C., S.J., D.K., G.M., J.I.M., L.W., and J.Y. also contributed to the writing of this paper.

Competing interests. The authors declare no conflict of interests.

Corresponding Author. Correspondance to Diana Powell.

Methods References

- [25] Bell, T. *et al.* Eureka!: An End-to-End Pipeline for JWST Time-Series Observations. *The Journal of Open Source Software* **7** (79), 4503 (2022) .
- [26] Bell, T. J. *et al.* A First Look at the JWST MIRI/LRS Phase Curve of WASP-43b. *arXiv e-prints* (2023). [arXiv:2301.06350](https://arxiv.org/abs/2301.06350) .
- [27] Bell, T. J., Crouzet, N. & et al. *in prep.* (2023) .
- [28] Bushouse, H. *et al.* Jwst calibration pipeline (2022). URL <https://doi.org/10.5281/zenodo.7325378>.
- [29] Argyriou, I. *et al.* The Brighter-Fatter Effect in the JWST MIRI Si:As IBC detectors I. Observations, impact on science, and modelling. *arXiv e-prints* (2023). [arXiv:2303.13517](https://arxiv.org/abs/2303.13517) .
- [30] Horne, K. An optimal extraction algorithm for CCD spectroscopy. *PASP* **98**, 609–617 (1986) .
- [31] Luger, R. *et al.* starry: Analytic Occultation Light Curves. *AJ* **157** (2), 64 (2019) .

- [32] Kipping, D. M. Efficient, uninformative sampling of limb darkening coefficients for two-parameter laws. *Mon. Not. R. Astron. Soc.* **435** (3), 2152–2160 (2013) .
- [33] Carter, A. L., May, E. M. & et al. *in prep.* (2023) .
- [34] Bouwman, J. *et al.* Spectroscopic Time Series Performance of the Mid-infrared Instrument on the JWST. *PASP* **135** (1045), 038002 (2023) .
- [35] Schlawin, E. *et al.* JWST NIRCam Defocused Imaging: Photometric Stability Performance and How It Can Sense Mirror Tilts. *PASP* **135** (1043), 018001 (2023) .
- [36] Salvatier, J., Wiecki, T. V. & Fonnesbeck, C. Probabilistic programming in python using pymc3. *PeerJ Computer Science* **2**, e55 (2016) .
- [37] Gelman, A. & Rubin, D. B. Inference from Iterative Simulation Using Multiple Sequences. *Statistical Science* **7**, 457–472 (1992) .
- [38] Morello, G. *et al.* The ExoTETHyS Package: Tools for Exoplanetary Transits around Host Stars. *AJ* **159** (2), 75 (2020) .
- [39] Morello, G. *et al.* ExoTETHyS: Tools for Exoplanetary Transits around host stars. *The Journal of Open Source Software* **5** (46), 1834 (2020) .
- [40] Chiavassa, A. *et al.* The STAGGER-grid: A grid of 3D stellar atmosphere models. V. Synthetic stellar spectra and broad-band photometry. *A&A* **611**, A11 (2018) .
- [41] Allan, D. W. Statistics of atomic frequency standards. *IEEE Proceedings* **54**, 221–230 (1966) .
- [42] Kirk, J. *et al.* Rayleigh scattering in the transmission spectrum of HAT-P-18b. *Mon. Not. R. Astron. Soc.* **468** (4), 3907–3916 (2017) .
- [43] Kirk, J. *et al.* LRG-BEASTS: Transmission Spectroscopy and Retrieval Analysis of the Highly Inflated Saturn-mass Planet WASP-39b. *Astron. J.* **158** (4), 144 (2019) .
- [44] Kirk, J. *et al.* ACCESS and LRG-BEASTS: A Precise New Optical Transmission Spectrum of the Ultrahot Jupiter WASP-103b. *Astron. J.* **162** (1), 34 (2021) .
- [45] The JWST Transiting Exoplanet Community Early Release Science Team *et al.* Identification of carbon dioxide in an exoplanet atmosphere. *Nature* arXiv:2208.11692 (2022) .

- 1254 [46] Alderson, L. *et al.* Early release science of the exoplanet wasp-39b with
1255 jwst nirspec g395h. *Nature* (2023) .
- 1256 [47] Rustamkulov, Z. *et al.* Early Release Science of the exoplanet WASP-39b
1257 with JWST NIRSpec PRISM. *Nature* **614** (7949), 659–663 (2023) .
- 1258 [48] Lustig-Yaeger, J. *et al.* A JWST transmission spectrum of a nearby
1259 Earth-sized exoplanet. *arXiv e-prints* arXiv:2301.04191 (2023) .
- 1260 [49] Kreidberg, L. batman: BAsic Transit Model cAlculatioN in Python.
1261 *PASP* **127** (957), 1161 (2015) .
- 1262 [50] Foreman-Mackey, D., Hogg, D. W., Lang, D. & Goodman, J. emcee:
1263 The MCMC Hammer. *PASP* **125** (925), 306 (2013) .
- 1264 [51] Kempton, E. M.-R. *et al.* A reflective, metal-rich atmosphere for gj 1214b
1265 from its jwst phase curve. *Nature* (2023) .
- 1266 [52] Lodders, K. Solar elemental abundances (2020).
- 1267 [53] Pacetti, E. *et al.* Chemical Diversity in Protoplanetary Disks and Its
1268 Impact on the Formation History of Giant Planets. *Astrophys. J.* **937** (1),
1269 36–57 (2022) .
- 1270 [54] Polanski, A. S., Crossfield, I. J. M., Howard, A. W., Isaacson, H. &
1271 Rice, M. Chemical Abundances for 25 JWST Exoplanet Host Stars with
1272 KeckSpec. *Research Notes of the American Astronomical Society* **6** (8),
1273 155 (2022) .
- 1274 [55] Tsai, S.-M. *et al.* Photochemically produced SO₂ in the atmosphere of
1275 WASP-39b. *Nature* **617** (7961), 483–487 (2023) .
- 1276 [56] Feinstein, A. D. *et al.* Early Release Science of the exoplanet WASP-39b
1277 with JWST NIRISS. *Nature* **614** (7949), 670–675 (2023) .
- 1278 [57] Ahrer, E.-M. *et al.* Early Release Science of the exoplanet WASP-39b
1279 with JWST NIRCam. *Nature* **614** (7949), 653–658 (2023) .
- 1280 [58] Tsai, S.-M. *et al.* VULCAN: an Open-Source, Validated Chemical Kinetics
1281 Python Code for Exoplanetary Atmospheres. *Astrophys. J. Suppl. Ser.* **228** (2), 1–26 (2017) .
- 1282 [59] Tsai, S.-M. *et al.* A comparative study of atmospheric chemistry with
VULCAN. *Astrophys. J.* **923** (2), 264–305 (2021) .
- 1283 [60] Moses, J. I. Sl9 impact chemistry: Long-term photochemical evolution.
1284 *International Astronomical Union Colloquium* **156**, 243–268 (1996) .

- 1287 [61] Zahnle, K., Marley, M. S., Morley, C. V. & Moses, J. I. Photolytic Hazes
1288 in the Atmosphere Of 51 Eri b. *Astrophys. J.* **824** (2), 137–153 (2016) .
- 1289 [62] Du, S., Francisco, J. S., Shepler, B. C. & Peterson, K. A. Determination
1290 of the rate constant for sulfur recombination by quasiclassical trajectory
1291 calculations. *JChPh* **128** (20), 204306–204306 (2008) .
- 1292 [63] Allen, M., Yung, Y. L. & Waters, J. W. Vertical transport and photo-
1293 chemistry in the terrestrial mesosphere and lower thermosphere (50–120
1294 km). *J. Geophys. Res.* **86**, 3617–3627 (1981) .
- 1295 [64] Yung, Y. L., Allen, M. & Pinto, J. P. Photochemistry of the atmosphere
1296 of Titan: Comparison between model and observations. *Astrophys. J.*
1297 *Suppl. Ser.* **55**, 465–506 (1984) .
- 1298 [65] Moses, J. I. *et al.* Disequilibrium carbon, oxygen, and nitrogen chemistry
1299 in the atmospheres of HD189733b and HD209458b. *Astrophys. J.* **737** (1)
1300 (2011) .
- 1301 [66] Moses, J. I. *et al.* Compositional diversity in the atmospheres of Hot
1302 Neptunes, with application to GJ 436b. *Astrophys. J.* **777** (1), 34–56
1303 (2013) .
- 1304 [67] Visscher, C. & Moses, J. I. Quenching of carbon monoxide and methane
1305 in the atmospheres of cool brown dwarfs and hot Jupiters. *Astrophys.*
1306 *J.* **738**, 72 (2011) .
- 1307 [68] Rimmer, P. B. & Helling, C. A Chemical Kinetics Network for Lightning
1308 and Life in Planetary Atmospheres. *ApJS* **224** (1), 9 (2016) .
- 1309 [69] Rimmer, P. B. & Rugheimer, S. Hydrogen cyanide in nitrogen-rich
1310 atmospheres of rocky exoplanets. *Icarus* **329**, 124–131 (2019) .
- 1311 [70] Rimmer, P. B. *et al.* Hydroxide Salts in the Clouds of Venus: Their Effect
1312 on the Sulfur Cycle and Cloud Droplet pH. *PSJ* **2** (4), 133 (2021) .
- 1313 [71] Hobbs, R., Rimmer, P. B., Shorttle, O. & Madhusudhan, N. Sulfur
1314 chemistry in the atmospheres of warm and hot Jupiters. *Mon. Not. R.*
1315 *Astron. Soc.* **506** (3), 3186–3204 (2021) .
- 1316 [72] Krasnopolsky, V. A. Chemical kinetic model for the lower atmosphere
1317 of Venus. *Icarus* **191** (1), 25–37 (2007) .
- 1318 [73] Zhang, X., Liang, M. C., Mills, F. P., Belyaev, D. A. & Yung, Y. L.
1319 Sulfur chemistry in the middle atmosphere of Venus. *Icarus* **217** (2),
1320 714–739 (2012) .

- 1321 [74] Hu, R., Seager, S. & Bains, W. Photochemistry in terrestrial exoplanet
1322 atmospheres. I. Photochemistry model and benchmark cases. *Astrophys.*
1323 **J.** **761** (2) (2012) .
- 1324 [75] Hu, R., Seager, S. & Bains, W. Photochemistry in terrestrial exoplanet
1325 atmospheres. II. H₂S and SO₂ photochemistry in anoxic atmospheres.
1326 *Astrophys. J.* **769** (1) (2013) .
- 1327 [76] Hu, R. & Seager, S. Photochemistry in terrestrial exoplanet atmospheres.
1328 III. Photochemistry and thermochemistry in thick atmospheres on super
1329 earths and mini neptunes. *Astrophys. J.* **784** (1) (2014) .
- 1330 [77] Hu, R. Information in the reflected-light spectra of widely separated
1331 giant exoplanets. *The Astrophysical Journal* **887** (2), 166 (2019) .
- 1332 [78] Hu, R. Photochemistry and spectral characterization of temperate and
1333 gas-rich exoplanets. *The Astrophysical Journal* **921** (1), 27 (2021) .
- 1334 [79] Hughes, K., Blitz, M. A., Pilling, M. J. & Robertson, S. H. A master
1335 equation model for the determination of rate coefficients in the h+so₂
1336 system. *Proc. Combust. Inst.* **29**, 2431–2437 (2002) .
- 1337 [80] Crossfield, I. J. M. Volatile-to-sulfur Ratios Can Recover a Gas Giant’s
1338 Accretion History. *ApJL* **952** (1), L18 (2023) .
- 1339 [81] Avni, Y. Energy spectra of X-ray clusters of galaxies. *Astrophys. J.* **210**,
1340 642–646 (1976) .
- 1341 [82] Schneider, A. D. & Bitsch, B. How drifting and evaporating pebbles
1342 shape giant planets. II. Volatiles and refractories in atmospheres. *A&A*
1343 **654**, A72 (2021) .
- 1344 [83] JWST Transiting Exoplanet Community Early Release Science Team
1345 *et al.* Identification of carbon dioxide in an exoplanet atmosphere. *Nature*
1346 **614** (7949), 649–652 (2023) .
- 1347 [84] Mukherjee, S., Moran, S. E., Ohno, K., Batalha, N. E. & Fortney, J. J.
1348 PICASO 3.0 Atmospheric Models of WASP-39 b for the JWST Tran-
1349 siting Exoplanet Community Early Release Science Program. Zenodo
1350 (2022).
- 1351 [85] Batalha, N. E., Marley, M. S., Lewis, N. K. & Fortney, J. J. Exoplanet
1352 Reflected-light Spectroscopy with PICASO. *Astrophys. J.* **878** (1), 70
1353 (2019) .
- 1354 [86] Mukherjee, S., Batalha, N. E., Fortney, J. J. & Marley, M. S. PICASO
1355 3.0: A One-dimensional Climate Model for Giant Planets and Brown

- 1356 Dwarfs. *Astrophys. J.* **942** (2), 71 (2023) .
- 1357 [87] Ackerman, A. S. & Marley, M. S. Precipitating Condensation Clouds in
1358 Substellar Atmospheres. *Astrophys. J.* **556** (2), 872–884 (2001) .
- 1359 [88] Rooney, C. M., Batalha, N. E., Gao, P. & Marley, M. S. A New Sedimentation Model for Greater Cloud Diversity in Giant Exoplanets and
1360 Brown Dwarfs. *Astrophys. J.* **925** (1), 33 (2022) .
- 1361 [89] Moses, J. I., Tremblin, P., Venot, O. & Miguel, Y. Chemical variation
1362 with altitude and longitude on exo-Neptunes: Predictions for Ariel phase-
1363 curve observations. *Experimental Astronomy* **53** (2), 279–322 (2022)
1364 .
- 1365 [90] Batalha, N., Freedman, R., Gharib-Nezhad, E. & Lupu, R. Resampled
1366 opacity database for picaso (2020). URL <https://doi.org/10.5281/zenodo.6928501>.
- 1367 [91] Heng, K. & Kitzmann, D. The theory of transmission spectra revisited:
1368 a semi-analytical method for interpreting WFC3 data and an unresolved
1371 challenge. *Mon. Not. R. Astron. Soc.* **470** (3), 2972–2981 (2017) .
- 1372 [92] Trotta, R. Bayes in the sky: Bayesian inference and model selection in
1373 cosmology. *Contemporary Physics* **49** (2), 71–104 (2008) .
- 1374 [93] Ormel, C. W. & Min, M. ARCiS framework for exoplanet atmospheres
1375 - the cloud transport model. *Astron. Astrophys.* **622**, A121 (2019) .
- 1376 [94] Min, M., Ormel, C. W., Chubb, K., Helling, C. & Kawashima, Y. The
1377 ARCiS framework for Exoplanet Atmospheres: Modelling Philosophy
1378 and Retrieval. *Astron. Astrophys.* **642**, A28 (2020) .
- 1379 [95] Feroz, F., Hobson, M. P. & Bridges, M. MULTINEST: an efficient and
1380 robust Bayesian inference tool for cosmology and particle physics. *Mon.*
1381 *Not. R. Astron. Soc.* **398** (4), 1601–1614 (2009) .
- 1382 [96] Woitke, P. *et al.* Equilibrium chemistry down to 100 K. Impact of silicates
1383 and phyllosilicates on the carbon to oxygen ratio. *Astron. Astrophys.*
1384 **614**, A1 (2018) .
- 1385 [97] Brady, R. P., Yurchenko, S. N., Kim, G.-S., Somogyi, W. & Tennyson,
1386 J. An ab initio study of the rovibronic spectrum of sulphur monoxide
1387 (SO): diabatic vs. adiabatic representation. *Phys. Chem. Chem. Phys.*
1388 **24**, 24076–24088 (2022) .
- 1389 [98] Underwood, D. S., Tennyson, J., Yurchenko, S. N., Clausen, S. & Fateev,
1390 A. ExoMol line lists XVII: A line list for hot SO₃. *Mon. Not. R. Astron.*

1391 *Soc.* **462**, 4300–4313 (2016) .

- 1392 [99] Yurchenko, S. N. *et al.* ExoMol Molecular linelists – XXIV: A new hot
1393 line list for silicon monohydride, SiH. *Mon. Not. R. Astron. Soc.* **473**,
1394 5324–5333 (2018) .
- 1395 [100] Darby-Lewis, D. *et al.* Synthetic spectra of BeH, BeD and BeT for
1396 emission modelling in JET plasmas. *J. Phys. B: At. Mol. Opt. Phys.* **51**,
1397 185701 (2018) .
- 1398 [101] Hargreaves, R. J. *et al.* Spectroscopic line parameters of NO, NO₂, and
1399 N₂O for the HITEMP database. *JQSRT* **232**, 35 – 53 (2019) .
- 1400 [102] Polyansky, O. L. *et al.* ExoMol molecular line lists XXX: a complete
1401 high-accuracy line list for water. *Mon. Not. R. Astron. Soc.* **480** (2),
1402 2597–2608 (2018) .
- 1403 [103] Underwood, D. S. *et al.* ExoMol molecular line lists - XIV. The rotation-
1404 vibration spectrum of hot SO₂. *Mon. Not. R. Astron. Soc.* **459** (4),
1405 3890–3899 (2016) .
- 1406 [104] Chubb, K. L. *et al.* The ExoMolOP database: Cross sections and k-tables
1407 for molecules of interest in high-temperature exoplanet atmospheres.
1408 *Astron. Astrophys.* **646**, A21 (2021) .
- 1409 [105] Tennyson, J. *et al.* The 2020 release of the exomol database: Molecular
1410 line lists for exoplanet and other hot atmospheres. *JQSRT* **255**, 107228
1411 (2020) .
- 1412 [106] Rothman, L. S. *et al.* HITEMP, the high-temperature molecular
1413 spectroscopic database. *JQSRT* **111**, 2139–2150 (2010) .
- 1414 [107] Borysow, A., Jorgensen, U. G. & Fu, Y. High-temperature (1000–7000
1415 K) collision-induced absorption of H₂ pairs computed from the first prin-
1416 ciples, with application to cool and dense stellar atmospheres. *JQSRT*
1417 **68**, 235–255 (2001) .
- 1418 [108] Borysow, A. Collision-induced absorption coefficients of H₂ pairs at
1419 temperatures from 60 K to 1000 K. *A&A* **390**, 779–782 (2002) .
- 1420 [109] Welbanks, L. & Madhusudhan, N. On Atmospheric Retrievals of Exo-
1421 planets with Inhomogeneous Terminators. *Astrophys. J.* **933** (1), 79
1422 (2022) .
- 1423 [110] Mikal-Evans, T. *et al.* Hubble Space Telescope Transmission Spec-
1424 troscopy for the Temperate Sub-Neptune TOI-270 d: A Possible
1425 Hydrogen-rich Atmosphere Containing Water Vapor. *Astron. J.* **165** (3),

1426 84 (2023) .

- 1427 [111] Welbanks, L. & Madhusudhan, N. Aurora: A Generalized Retrieval
1428 Framework for Exoplanetary Transmission Spectra. *Astrophys. J.*
1429 **913** (2), 114 (2021) .
- 1430 [112] Skilling, J. Fischer, R., Preuss, R. & Toussaint, U. V. (eds) *Nested*
1431 *Sampling*. (eds Fischer, R., Preuss, R. & Toussaint, U. V.) *Bayesian*
1432 *Inference and Maximum Entropy Methods in Science and Engineering: 24th International Workshop on Bayesian Inference and Maximum*
1433 *Entropy Methods in Science and Engineering*, Vol. 735 of *American*
1434 *Institute of Physics Conference Series*, 395–405 (2004).
- 1435 [113] Feroz, F., Hobson, M. P. & Bridges, M. MULTINEST: an efficient and
1436 robust Bayesian inference tool for cosmology and particle physics. *Mon.*
1437 *Not. R. Astron. Soc.* **398**, 1601–1614 (2009) .
- 1438 [114] Buchner, J. *et al.* X-ray spectral modelling of the AGN obscuring region
1439 in the CDFS: Bayesian model selection and catalogue. *A&A* **564**, A125
1440 (2014) .
- 1441 [115] Welbanks, L. & Madhusudhan, N. On Degeneracies in Retrievals of
1442 Exoplanetary Transmission Spectra. *Astron. J.* **157** (5), 206 (2019) .
- 1443 [116] Madhusudhan, N. & Seager, S. A Temperature and Abundance Retrieval
1444 Method for Exoplanet Atmospheres. *Astrophys. J.* **707** (1), 24–39 (2009)
1445 .
- 1446 [117] Barstow, J. K. Unveiling cloudy exoplanets: the influence of cloud model
1447 choices on retrieval solutions. *Mon. Not. R. Astron. Soc.* **497** (4), 4183–
1448 4195 (2020) .
- 1449 [118] Benneke, B. & Seager, S. How to Distinguish between Cloudy Mini-
1450 Neptunes and Water/Volatile-dominated Super-Earths. *Astrophys. J.*
1451 **778** (2), 153 (2013) .
- 1452 [119] Richard, C. *et al.* New section of the HITRAN database: Collision-
1453 induced absorption (CIA). *JQSRT* **113**, 1276–1285 (2012) .
- 1454 [120] MacDonald, R. J. & Madhusudhan, N. HD 209458b in new light: evi-
1455 dence of nitrogen chemistry, patchy clouds and sub-solar water. *Mon.*
1456 *Not. R. Astron. Soc.* **469** (2), 1979–1996 (2017) .
- 1457 [121] Line, M. R. *et al.* A Systematic Retrieval Analysis of Secondary
1458 Eclipse Spectra. I. A Comparison of Atmospheric Retrieval Techniques.
1459 *Astrophys. J.* **775** (2), 137 (2013) .
- 1460

- 1461 [122] Line, M. R. *et al.* Uniform Atmospheric Retrieval Analysis of Ultracool
1462 Dwarfs. II. Properties of 11 T dwarfs. *Astrophys. J.* **848** (2), 83 (2017) .
- 1463 [123] May, E. M., Taylor, J., Komacek, T. D., Line, M. R. & Parmentier, V.
1464 Water Ice Cloud Variability and Multi-epoch Transmission Spectra of
1465 TRAPPIST-1e. *ApJL* **911** (2), L30 (2021) .
- 1466 [124] Lacis, A. A. & Oinas, V. A description of the correlated-k distribution
1467 method for modelling nongray gaseous absorption, thermal emission,
1468 and multiple scattering in vertically inhomogeneous atmospheres.
1469 *J. Geophys. Res.* **96**, 9027–9064 (1991) .
- 1470 [125] Mollière, P., van Boekel, R., Dullemond, C., Henning, T. & Mordasini,
1471 C. Model Atmospheres of Irradiated Exoplanets: The Influence of Stellar
1472 Parameters, Metallicity, and the C/O Ratio. *Astrophys. J.* **813** (1), 47
1473 (2015) .
- 1474 [126] Mai, C. & Line, M. R. Exploring Exoplanet Cloud Assumptions in JWST
1475 Transmission Spectra. *Astrophys. J.* **883** (2), 144 (2019) .
- 1476 [127] Parmentier, V. & Guillot, T. A non-grey analytical model for irradiated
1477 atmospheres. I. Derivation. *A&A* **562**, A133 (2014) .
- 1478 [128] Lecavelier Des Etangs, A., Pont, F., Vidal-Madjar, A. & Sing, D.
1479 Rayleigh scattering in the transit spectrum of HD 189733b. *A&A*
1480 **481** (2), L83–L86 (2008) .
- 1481 [129] Line, M. R. *et al.* No Thermal Inversion and a Solar Water Abundance
1482 for the Hot Jupiter HD 209458b from HST/WFC3 Spectroscopy. *Astron.*
1483 *J.* **152** (6), 203 (2016) .
- 1484 [130] Kitzmann, D. *et al.* Helios-r2: A New Bayesian, Open-source Retrieval
1485 Model for Brown Dwarfs and Exoplanet Atmospheres. *Astrophys. J.*
1486 **890** (2), 174 (2020) .
- 1487 [131] Bourrier, V. *et al.* Optical phase curve of the ultra-hot Jupiter WASP-
1488 121b. *A&A* **637**, A36 (2020) .
- 1489 [132] Mesa, D. *et al.* Characterizing brown dwarf companions with IRDIS long-
1490 slit spectroscopy: HD 1160 B and HD 19467 B. *Mon. Not. R. Astron.*
1491 *Soc.* **495** (4), 4279–4290 (2020) .
- 1492 [133] Lueber, A., Kitzmann, D., Bowler, B. P., Burgasser, A. J. & Heng, K.
1493 Retrieval Study of Brown Dwarfs across the L-T Sequence. *Astrophys.*
1494 *J.* **930** (2), 136 (2022) .

- 1495 [134] Stock, J. W., Kitzmann, D., Patzer, A. B. C. & Sedlmayr, E. FastChem:
1496 A computer program for efficient complex chemical equilibrium calcula-
1497 tions in the neutral/ionized gas phase with applications to stellar and
1498 planetary atmospheres. *Mon. Not. R. Astron. Soc.* **479** (1), 865–874
1499 (2018) .
- 1500 [135] Stock, J. W., Kitzmann, D. & Patzer, A. B. C. FASTCHEM 2 : an
1501 improved computer program to determine the gas-phase chemical equi-
1502 librium composition for arbitrary element distributions. *Mon. Not. R.*
1503 *Astron. Soc.* **517** (3), 4070–4080 (2022) .
- 1504 [136] Harris, G. J., Tennyson, J., Kaminsky, B. M., Pavlenko, Y. V. & Jones,
1505 H. R. A. Improved HCN/HNC linelist, model atmospheres and synthetic
1506 spectra for WZ Cas. *Mon. Not. R. Astron. Soc.* **367** (1), 400–406 (2006)
1507 .
- 1508 [137] Li, G. *et al.* Rovibrational Line Lists for Nine Isotopologues of the CO
1509 Molecule in the X $^1\Sigma^+$ Ground Electronic State. *ApJS* **216** (1), 15
1510 (2015) .
- 1511 [138] Yurchenko, S. N., Amundsen, D. S., Tennyson, J. & Waldmann, I. P. A
1512 hybrid line list for CH₄ and hot methane continuum. *A&A* **605**, A95
1513 (2017) .
- 1514 [139] Grimm, S. L. & Heng, K. HELIOS-K: An Ultrafast, Open-source Opacity
1515 Calculator for Radiative Transfer. *Astrophys. J.* **808** (2), 182 (2015) .
- 1516 [140] Grimm, S. L. *et al.* HELIOS-K 2.0 Opacity Calculator and Open-source
1517 Opacity Database for Exoplanetary Atmospheres. *ApJS* **253** (1), 30
1518 (2021) .
- 1519 [141] Abel, M., Frommhold, L., Li, X. & Hunt, K. L. C. Collision-Induced
1520 Absorption by H₂Pairs: From Hundreds to Thousands of Kelvin. *Journal*
1521 *of Physical Chemistry A* **115** (25), 6805–6812 (2011) .
- 1522 [142] Abel, M., Frommhold, L., Li, X. & Hunt, K. L. C. Infrared absorption
1523 by collisional H₂-He complexes at temperatures up to 9000 K and fre-
1524 quencies from 0 to 20 000 cm⁻¹. *JChPh* **136** (4), 044319–044319 (2012)
1525 .
- 1526 [143] Fletcher, L. N., Gustafsson, M. & Orton, G. S. Hydrogen Dimers in
1527 Giant-planet Infrared Spectra. *ApJS* **235** (1), 24 (2018) .
- 1528 [144] Irwin, P. G. J. *et al.* The NEMESIS planetary atmosphere radiative
1529 transfer and retrieval tool. *JQSRT* **109**, 1136–1150 (2008) .

- 1530 [145] Krissansen-Totton, J., Garland, R., Irwin, P. & Catling, D. C.
1531 Detectability of Biosignatures in Anoxic Atmospheres with the James
1532 Webb Space Telescope: A TRAPPIST-1e Case Study. *Astron. J.* **156** (3),
1533 114 (2018) .
- 1534 [146] Rodgers, C. D. Inverse Methods for Atmospheric Sounding - Theory
1535 and Practice. Inverse Methods for Atmospheric Sounding - Theory and
1536 Practice. Series: Series on Atmospheric Oceanic and Planetary Physics,
1537 ISBN: 9789812813718. World Scientific Publishing Co. Pte. Ltd., Edited
1538 by Clive D. Rodgers, vol. 2 (2000).
- 1539 [147] Irwin, P. G. J. *et al.* 2.5D retrieval of atmospheric properties from exo-
1540 planet phase curves: application to WASP-43b observations. *Mon. Not.*
1541 *R. Astron. Soc.* **493** (1), 106–125 (2020) .
- 1542 [148] Cubillos, P. E. & Blecic, J. The Pyrat Bay Framework for Exo-
1543 planet Atmospheric Modeling: A Population Study of Hubble/WFC3
1544 Transmission Spectra. *Mon. Not. R. Astron. Soc.* (2021) .
- 1545 [149] Burrows, A., Marley, M. S. & Sharp, C. M. The Near-Infrared and
1546 Optical Spectra of Methane Dwarfs and Brown Dwarfs. *Astrophys. J.*
1547 **531**, 438–446 (2000) .
- 1548 [150] Kurucz, R. L. Atlas: a Computer Program for Calculating Model Stellar
1549 Atmospheres. *SAO Special Report* **309** (1970) .
- 1550 [151] Lecavelier Des Etangs, A., Pont, F., Vidal-Madjar, A. & Sing, D.
1551 Rayleigh scattering in the transit spectrum of HD 189733b. *A&A*
1552 **481** (2), L83–L86 (2008) .
- 1553 [152] Tennyson, J. *et al.* The ExoMol database: Molecular line lists for exo-
1554 planet and other hot atmospheres. *Journal of Molecular Spectroscopy*
1555 **327**, 73–94 (2016) .
- 1556 [153] Cubillos, P. E. An Algorithm to Compress Line-transition Data for
1557 Radiative-transfer Calculations. *Astrophys. J.* **850** (1), 32 (2017) .
- 1558 [154] Line, M. R. & Parmentier, V. The Influence of Nonuniform Cloud Cover
1559 on Transit Transmission Spectra. *Astrophys. J.* **820**, 78 (2016) .
- 1560 [155] Blecic, J., Baker, A., Cubillos, P., Dobbs-Dixon, S. & Greene, T. The
1561 Thermal Stability Cloud Model for Retrieval. *in prep* (2023) .
- 1562 [156] Kilpatrick, B. M. *et al.* Community Targets of JWST's Early Release
1563 Science Program: Evaluation of WASP-63b. *Astron. J.* **156** (3), 103
1564 (2018) .

- 1565 [157] Venot, O. *et al.* Global Chemistry and Thermal Structure Models for
1566 the Hot Jupiter WASP-43b and Predictions for JWST. *Astrophys. J.*
1567 **890** (2), 176 (2020) .
- 1568 [158] Blecic, J., Harrington, J. & Bowman, M. O. TEA: A Code Calculating
1569 Thermochemical Equilibrium Abundances. *ApJS* **225**, 4 (2016) .
- 1570 [159] J., B. TEA Documentation. <https://github.com/dzesmin/TEA> (2017).
1571 [Online].
- 1572 [160] Cubillos, P. E., Blecic, J. & Dobbs-Dixon, I. Toward More Reliable Analytic
1573 Thermochemical-equilibrium Abundances. *Astrophys. J.* **872** (1),
1574 111 (2019) .
- 1575 [161] ter Braak, C. J. F. & Vrugt, J. A. Differential evolution markov chain
1576 with snooker updater and fewer chains. *Statistics and Computing* **18** (4),
1577 435–446 (2008) .
- 1578 [162] Cubillos, P. *et al.* On Correlated-noise Analyses Applied to Exoplanet
1579 Light Curves. *Astron. J.* **153** (1), 3 (2017) .
- 1580 [163] Buchner, J. *et al.* X-ray spectral modelling of the AGN obscuring region
1581 in the CDFS: Bayesian model selection and catalogue. *Astronomy and*
1582 *Astrophysics* **564**, A125 (2014) .
- 1583 [164] Hargreaves, R. J. *et al.* An Accurate, Extensive, and Practical Line List
1584 of Methane for the HITEMP Database. *ApJS* **247** (2), 55 (2020) .
- 1585 [165] Yurchenko, S. N., Barber, R. J. & Tennyson, J. A variationally computed
1586 line list for hot NH₃. *Mon. Not. R. Astron. Soc.* **413** (3), 1828–1834
1587 (2011) .
- 1588 [166] Yurchenko, S. N. A theoretical room-temperature line list for ¹⁵NH₃.
1589 *JQSRT* **152**, 28–36 (2015) .
- 1590 [167] Harris, G. J. *et al.* A H¹³CN/HN¹³C linelist, model atmospheres and
1591 synthetic spectra for carbon stars. *Mon. Not. R. Astron. Soc.* **390** (1),
1592 143–148 (2008) .
- 1593 [168] Rothman, L. S. *et al.* HITEMP, the high-temperature molecular
1594 spectroscopic database. *JQSRT* **111**, 2139–2150 (2010) .
- 1595 [169] Wilzewski, J. S., Gordon, I. E., Kochanov, R. V., Hill, C. & Rothman,
1596 L. S. H₂, he, and co₂ line-broadening coefficients, pressure shifts and
1597 temperature-dependence exponents for the hitran database. part 1: So₂,
1598 nh₃, hf, hcl, ocs and c₂h₂. *Journal of Quantitative Spectroscopy and*
1599 *Radiative Transfer* **168**, 193–206 (2016) .

- 1600 [170] Azzam, A. A. A., Tennyson, J., Yurchenko, S. N. & Naumenko, O. V.
1601 ExoMol molecular line lists – XVI. The rotation–vibration spectrum of
1602 hot H₂S. *Monthly Notices of the Royal Astronomical Society* **460** (4),
1603 4063–4074 (2016) .
- 1604 [171] Borysow, A., Jorgensen, U. G. & Fu, Y. High-temperature (1000–7000
1605 K) collision-induced absorption of H₂ pairs computed from the first prin-
1606 ciples, with application to cool and dense stellar atmospheres. *JQSRT*
1607 **68**, 235–255 (2001) .
- 1608 [172] Waldmann, I. P. *et al.* Tau-REx I: A Next Generation Retrieval Code
1609 for Exoplanetary Atmospheres. *Astrophys. J.* **802** (2), 107 (2015) .
- 1610 [173] Waldmann, I. P. *et al.* Tau-REx II: Retrieval of Emission Spectra.
1611 *Astrophys. J.* **813** (1), 13 (2015) .
- 1612 [174] Al-Refaie, A. F., Changeat, Q., Waldmann, I. P. & Tinetti, G. TauREx 3:
1613 A Fast, Dynamic, and Extendable Framework for Retrievals. *Astrophys.*
1614 *J.* **917** (1), 37 (2021) .
- 1615 [175] Al-Refaie, A. F., Changeat, Q., Venot, O., Waldmann, I. P. & Tinetti, G.
1616 A Comparison of Chemical Models of Exoplanet Atmospheres Enabled
1617 by TauREx 3.1. *Astrophys. J.* **932** (2), 123 (2022) .
- 1618 [176] Barber, R. J. *et al.* ExoMol line lists - III. An improved hot rotation-
1619 vibration line list for HCN and HNC. *Mon. Not. R. Astron. Soc.* **437** (2),
1620 1828–1835 (2014) .
- 1621 [177] Coles, P. A., Yurchenko, S. N. & Tennyson, J. ExoMol molecular line
1622 lists - XXXV. A rotation-vibration line list for hot ammonia. *Mon. Not.*
1623 *R. Astron. Soc.* **490** (4), 4638–4647 (2019) .
- 1624 [178] Wende, S., Reiners, A., Seifahrt, A. & Bernath, P. F. CRIRES
1625 spectroscopy and empirical line-by-line identification of FeH molecular
1626 absorption in an M dwarf. *A&A* **523**, A58 (2010) .
- 1627 [179] Lee, J.-M., Heng, K. & Irwin, P. G. J. Atmospheric Retrieval Analysis
1628 of the Directly Imaged Exoplanet HR 8799b. *Astrophys. J.* **778** (2), 97
1629 (2013) .
- 1630 [180] Lee, E. K. H. *et al.* 3D Radiative Transfer for Exoplanet Atmospheres.
1631 gCMCRT: A GPU-accelerated MCRT Code. *Astrophys. J.* **929** (2),
1632 180–194 (2022) .
- 1633 [181] Harris, C. R. *et al.* Array programming with NumPy. *Nature* **585** (7825),
1634 357–362 (2020) .

- 1635 [182] Astropy Collaboration *et al.* Astropy: A community Python package for
1636 astronomy. *A&A* **558**, A33 (2013) .
- 1637 [183] Astropy Collaboration *et al.* The Astropy Project: Building an Open-
1638 science Project and Status of the v2.0 Core Package. *AJ* **156** (3), 123
1639 (2018) .
- 1640 [184] Hunter, J. D. Matplotlib: A 2d graphics environment. *Computing in
1641 Science & Engineering* **9** (3), 90–95 (2007) .

1642 Author Affiliations

- 1643
1644 ¹Center for Astrophysics | Harvard & Smithsonian, Cambridge, USA.
1645 ²Department of Astronomy & Astrophysics, University of Chicago,
1646 Chicago, IL, USA.
1647 ³Laboratory for Atmospheric and Space Physics, University of Colorado
1648 Boulder, UCB 600, Boulder, CO 80309.
1649 ⁴Center for Space and Habitability, University of Bern, Bern, Switzerland.
1650 ⁵51 Pegasi b fellow.
1651 ⁶Department of Earth Sciences, University of California, Riverside, Cali-
1652 fornia, USA.
1653 ⁷Department of Physics, University of Oxford, Oxford, UK.
1654 ⁸Institut Trottier de Recherche sur les Exoplanètes and Département de
1655 Physique, Université de Montréal, Montréal, QC, Canada.
1656 ⁹Department of Physics, Imperial College London, London, UK.
1657 ¹⁰Bay Area Environmental Research Institute, NASA Ames Research
1658 Center, Moffett Field, CA, USA.
1659 ¹¹Space Science and Astrobiology Division, NASA Ames Research Center,
1660 Moffett Field, CA, USA.
1661 ¹²School of Physical Sciences, The Open University, Milton Keynes, UK.
1662 ¹³Earth and Planets Laboratory, Carnegie Institution for Science, Wash-
1663 ington, DC, USA.
1664 ¹⁴Department of Physics, New York University Abu Dhabi, Abu Dhabi,
1665 UAE.
1666 ¹⁵Center for Astro, Particle and Planetary Physics (CAP3), New York
1667 University Abu Dhabi, Abu Dhabi, UAE.
1668 ¹⁶Centre for Exoplanet Science, University of St Andrews, St Andrews, UK.
1669 ¹⁷Department of Physics & Astronomy, University of Kansas, Lawrence,
1670 KS, USA.
1671 ¹⁸Institute of Astronomy, University of Cambridge, Cambridge, UK.
1672 ¹⁹Lunar and Planetary Laboratory, University of Arizona, Tucson, AZ,
1673 USA.
1674 ²⁰Department of Space, Earth and Environment, Chalmers University of
1675 Technology, Gothenburg, Sweden.
1676 ²¹Instituto de Astrofísica de Canarias (IAC), Tenerife, Spain.

- 1677 ²²INAF–Palermo Astronomical Observatory, Piazza del Parlamento,
1678 Palermo, Italy.
- 1679 ²³Space Science Institute, Boulder, CO, USA.
- 1680 ²⁴School of Earth and Space Exploration, Arizona State University, Tempe,
1681 AZ, USA.
- 1682 ²⁵NHFP Sagan Fellow.
- 1683 ²⁶Planetary Sciences Section, Jet Propulsion Laboratory, California Insti-
1684 tute of Technology, Pasadena, USA.
- 1685 ²⁷Department of Earth and Planetary Sciences, University of California
1686 Santa Cruz, Santa Cruz, California, USA.
- 1687 ²⁸Centre for Exoplanets and Habitability, University of Warwick, Coventry,
1688 UK.
- 1689 ²⁹Department of Physics, University of Warwick, Coventry, UK.
- 1690 ³⁰Astrophysics Section, Jet Propulsion Laboratory, California Institute of
1691 Technology, Pasadena, CA, USA.
- 1692 ³¹School of Physics and Astronomy, University of Leicester, Leicester.
- 1693 ³²Leiden Observatory, University of Leiden, Leiden, The Netherlands.
- 1694 ³³INAF - Turin Astrophysical Observatory, Pino Torinese, Italy.
- 1695 ³⁴Space Research Institute, Austrian Academy of Sciences, Graz, Austria.
- 1696 ³⁵Space and Planetary Sciences, Institute of Physics, University of Bern.
- 1697 ³⁶Université Paris-Saclay, CEA, CNRS, AIM, Gif-sur-Yvette, France.
- 1698 ³⁷Department of Astronomy and Carl Sagan Institute, Cornell University,
1699 Ithaca, NY, USA.
- 1700 ³⁸Division of Geological and Planetary Sciences, California Institute of
1701 Technology, Pasadena, CA, USA.
- 1702 ³⁹Max Planck Institute for Astronomy, Heidelberg, Germany.
- 1703 ⁴⁰SRON Netherlands Institute for Space Research, Leiden, the Nether-
1704 lands.
- 1705 ⁴¹Université Côte d’Azur, Observatoire de la Côte d’Azur, CNRS, Labora-
1706 toire Lagrange, France.
- 1707 ⁴²Department of Earth, Atmospheric and Planetary Sciences, Mas-
1708 sachusetts Institute of Technology, Cambridge, MA, USA.
- 1709 ⁴³Kavli Institute for Astrophysics and Space Research, Massachusetts
1710 Institute of Technology, Cambridge, MA, USA.
- 1711 ⁴⁴Astronomy Department and Van Vleck Observatory, Wesleyan Univer-
1712 sity, Middletown, CT, USA.
- 1713 ⁴⁵Johns Hopkins Applied Physics Laboratory, Laurel, MD, USA.
- 1714 ⁴⁶School of Physics, University of Bristol, Bristol, UK.
- 1715 ⁴⁷Indian Institute of Technology, Indore, India.
- 1716 ⁴⁸Department of Astronomy & Astrophysics, University of California,
1717 Santa Cruz, Santa Cruz, CA, USA.
- 1718 ⁴⁹NASA Ames Research Center, Moffett Field, CA, USA.
- 1719 ⁵⁰Department of Astrophysical and Planetary Sciences, University of
1720 Colorado, Boulder, CO, USA.

1721 ⁵¹Department of Physics and Astronomy, University College London,
1722 United Kingdom.

1723 ⁵²Instituto de Astrofisica, Facultad Ciencias Exactas, Universidad Andres
1724 Bello, Santiago, Chile.

1725 ⁵³Centro de Astrofisica y Tecnologias Afines (CATA), Casilla 36-D, Santi-
1726 ago, Chile.

1727 ⁵⁴Nucleo Milenio de Formacion Planetaria (NPF), Chile.

1728 ⁵⁵Anton Pannekoek Institute for Astronomy, University of Amsterdam,
1729 Amsterdam, The Netherlands.

1730 ⁵⁶Planetary Sciences Group, Department of Physics and Florida Space
1731 Institute, University of Central Florida, Orlando, Florida, USA.

1732 ⁵⁷Institute of Planetary research, German aerospace center (DLR), Berlin,
1733 Germany.

1734 ⁵⁸Department of Physics, Utah Valley University, Orem, UT, USA.

1735 ⁵⁹Department of Astronomy, University of Michigan, Ann Arbor, MI, USA.

1736 ⁶⁰Department of Physics, University of Rome ‘Tor Vergata’, Rome, Italy.

1737 ⁶¹Universitäts-Sternwarte, Ludwig-Maximilians-Universität München,
1738 München, Germany.

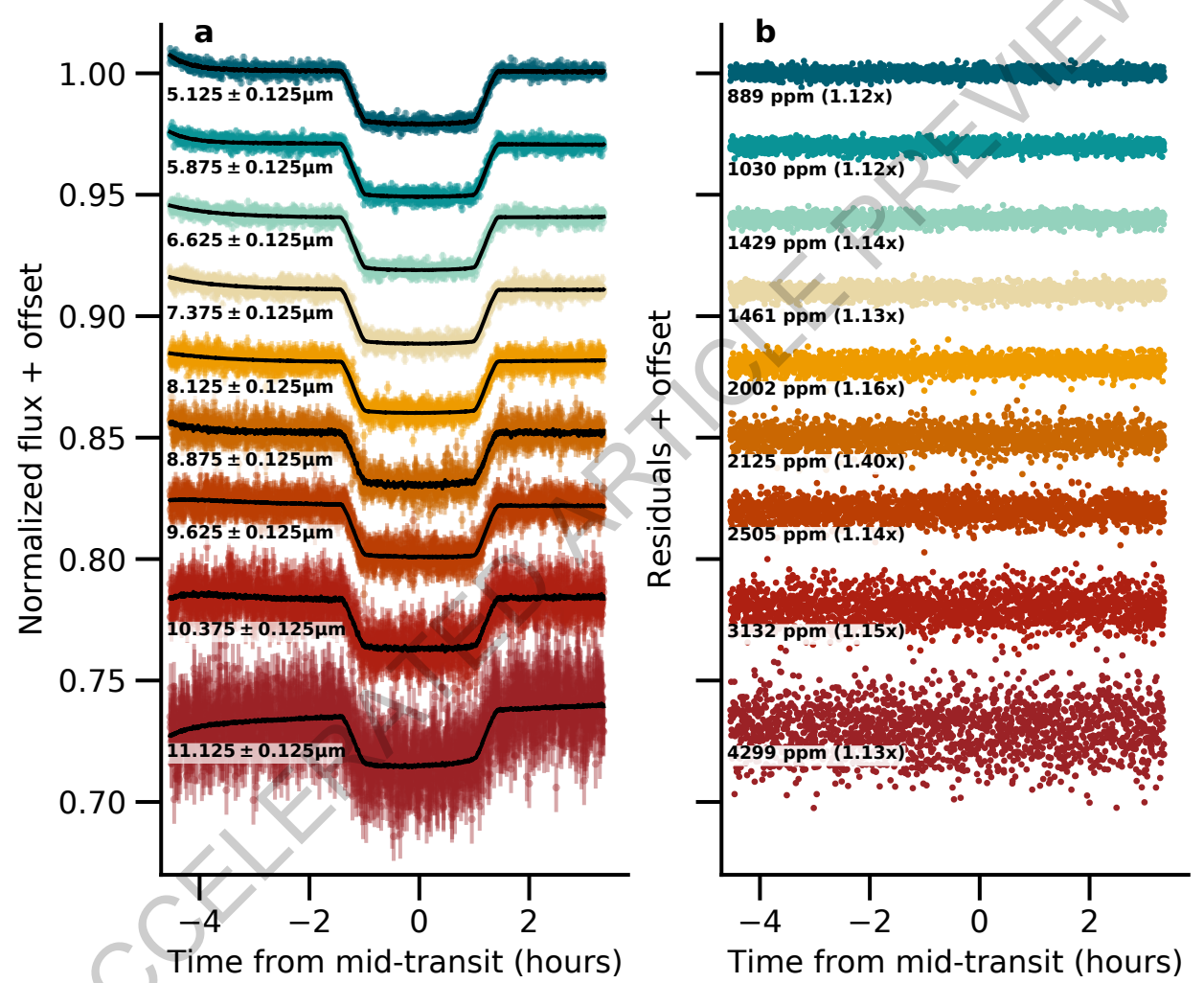
1739 ⁶²Exzellenzcluster Origins, Garching, Germany.

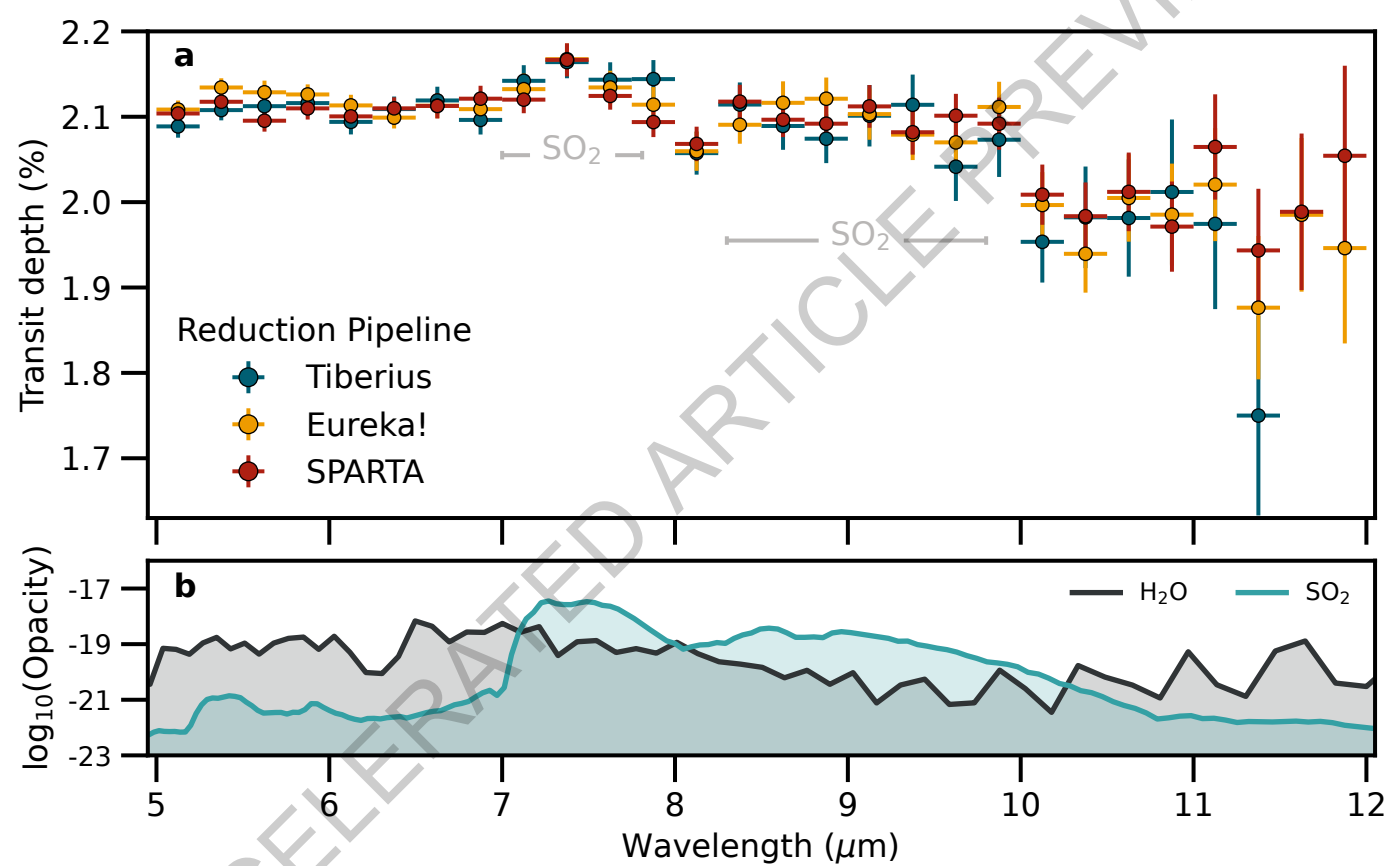
1740 ⁶³Department of Astronomy, University of Maryland, College Park, MD,
1741 USA.

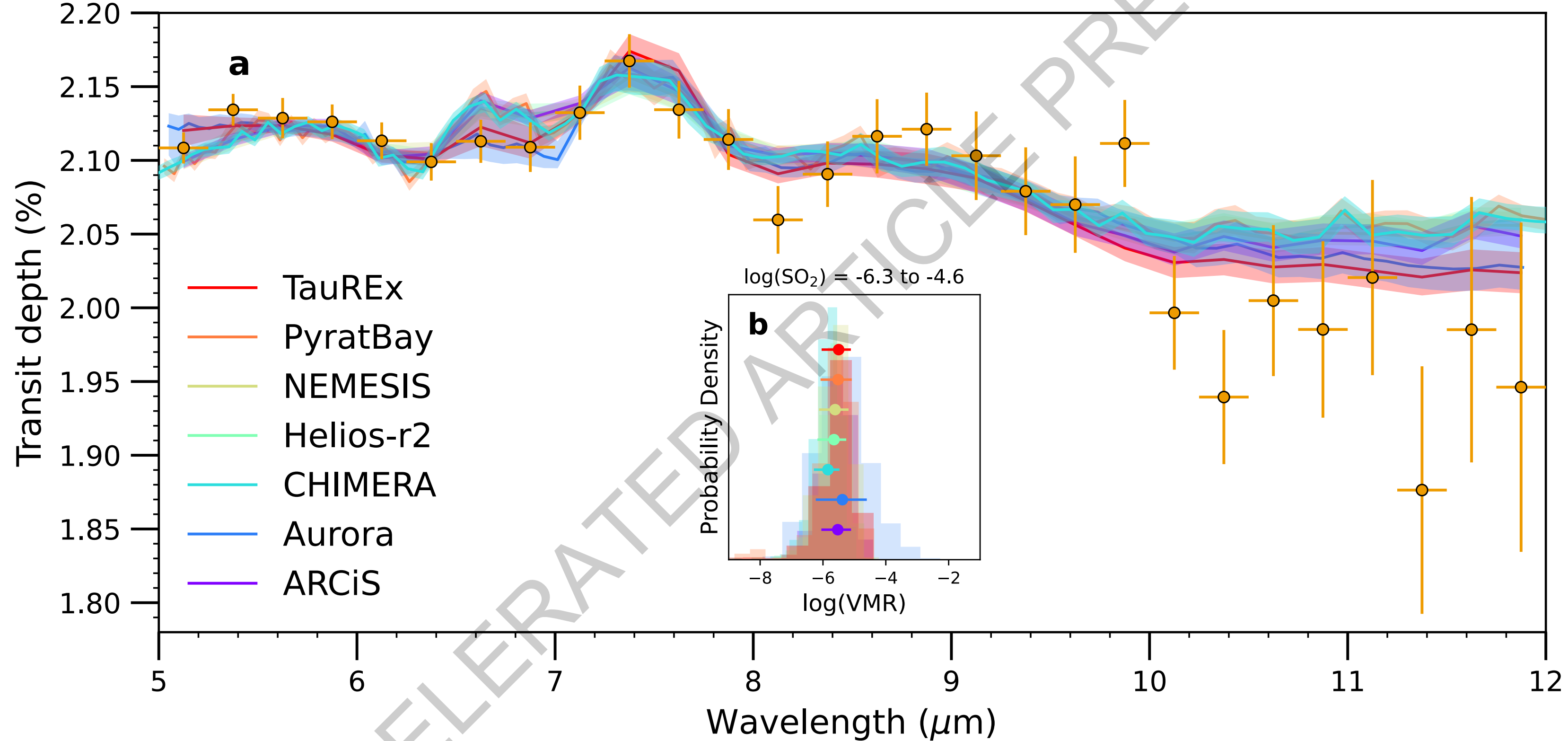
1742 ⁶⁴Department of Earth and Planetary Sciences, Johns Hopkins University,
1743 Baltimore, MD, USA.

1744 ⁶⁵Department of Physics & Astronomy, Johns Hopkins University, Balti-
1745 more, MD, USA.

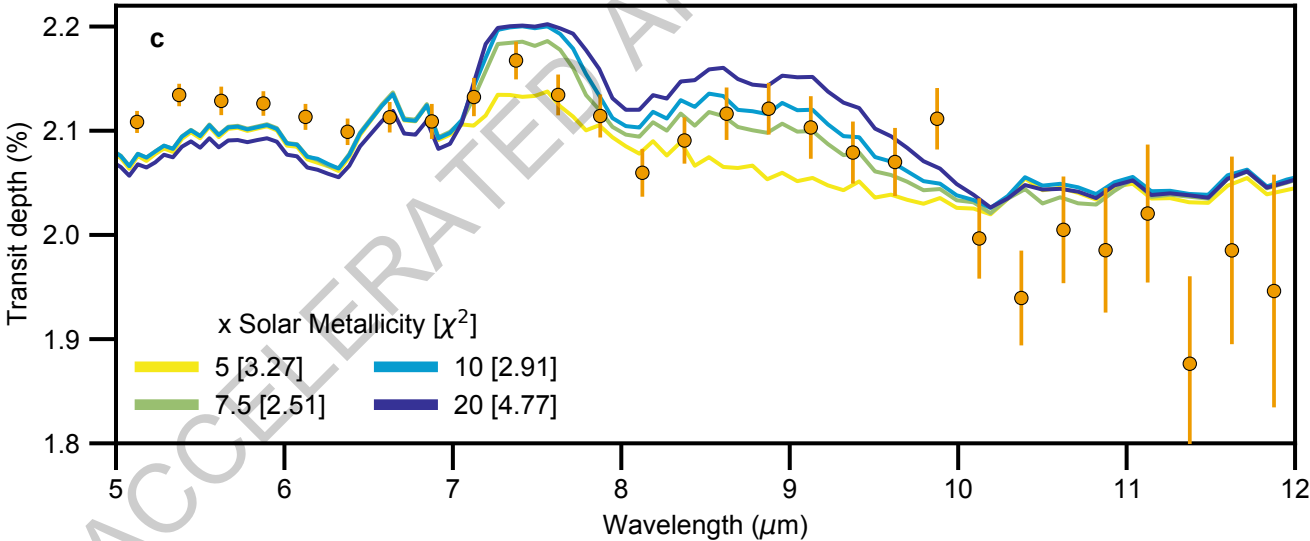
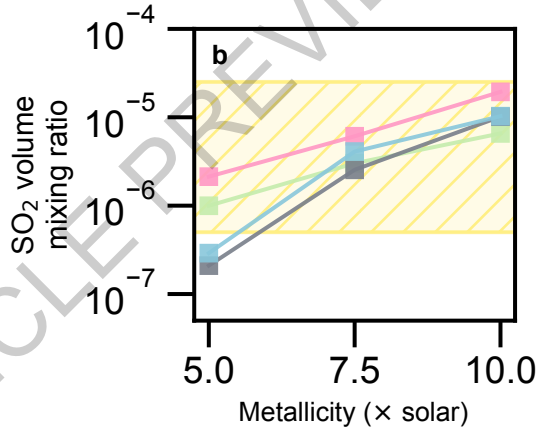
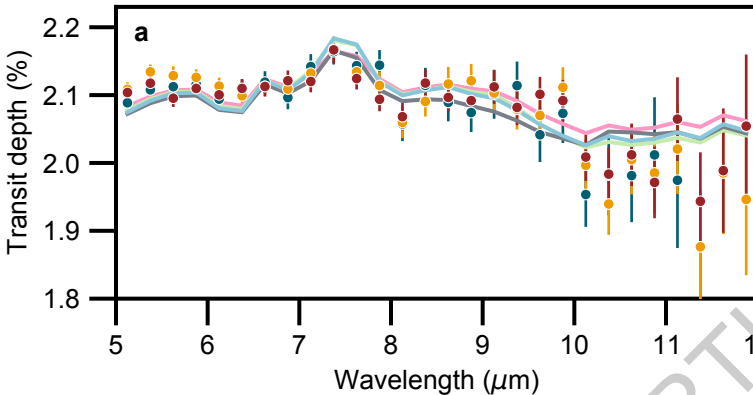
1746 ⁶⁶Université de Paris Cité and Univ Paris Est Creteil, CNRS, LISA, Paris,
1747 France.

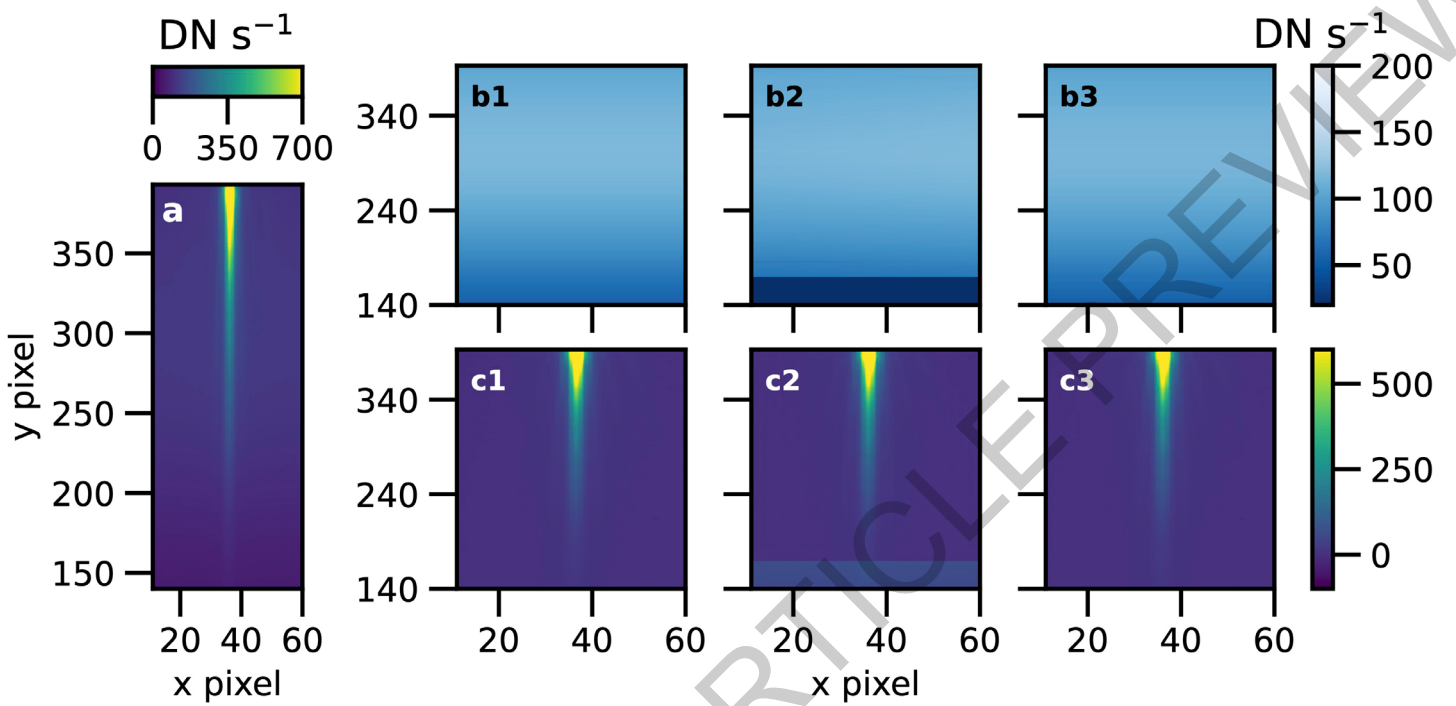




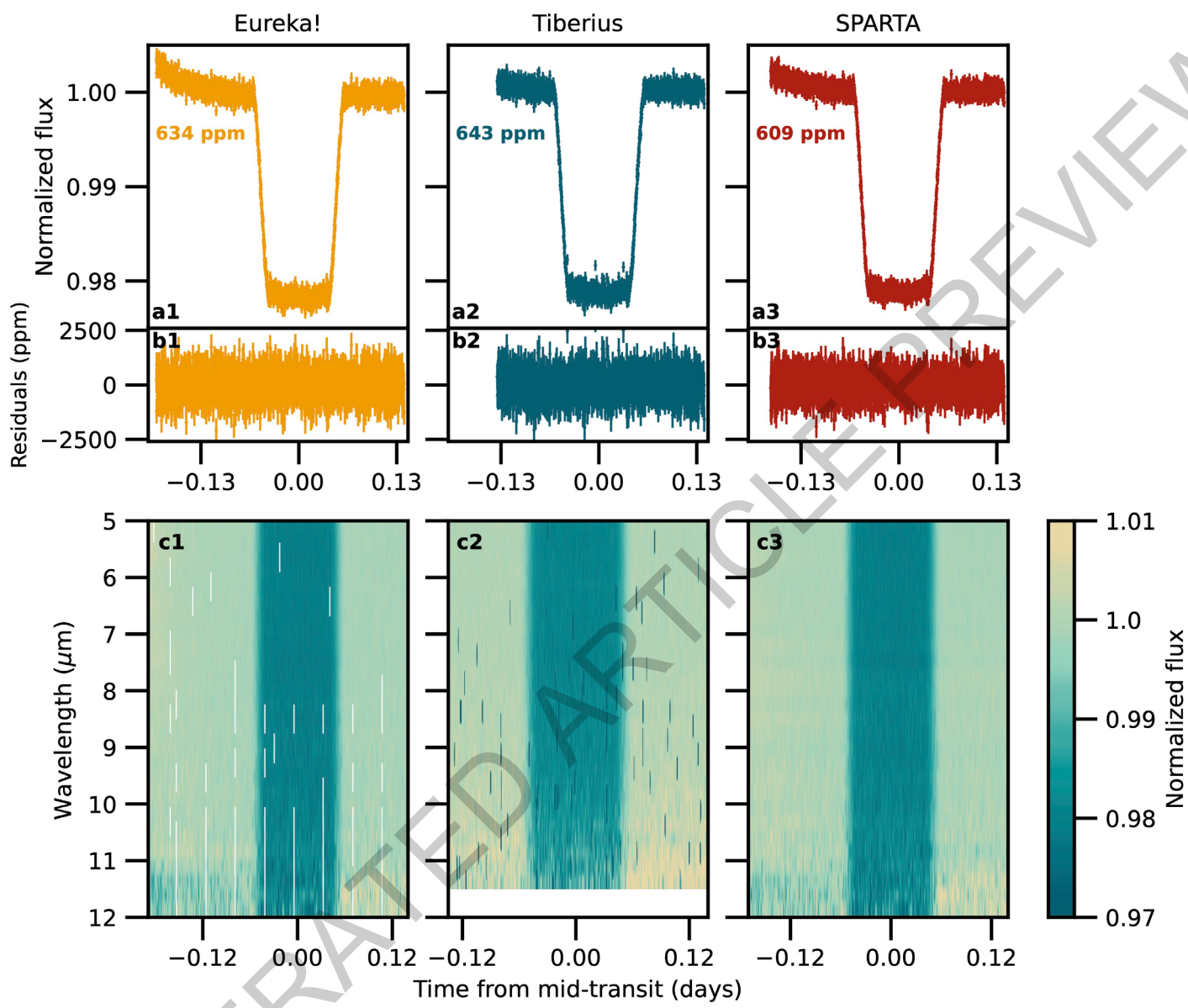


● Tiberius ● Eureka! ● SPARTA
— ARGO — EPACRIS — KINETICS — VULCAN

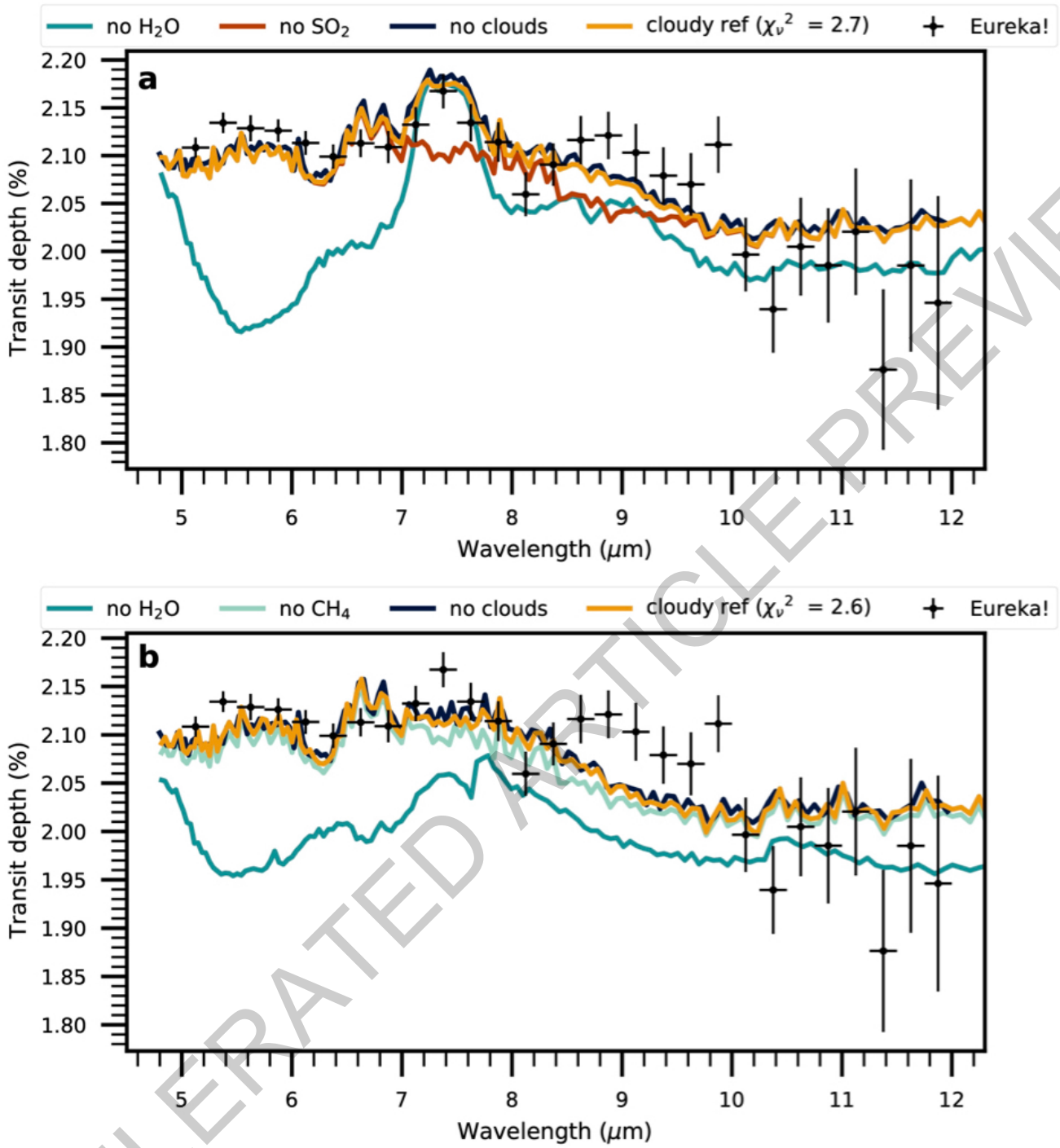




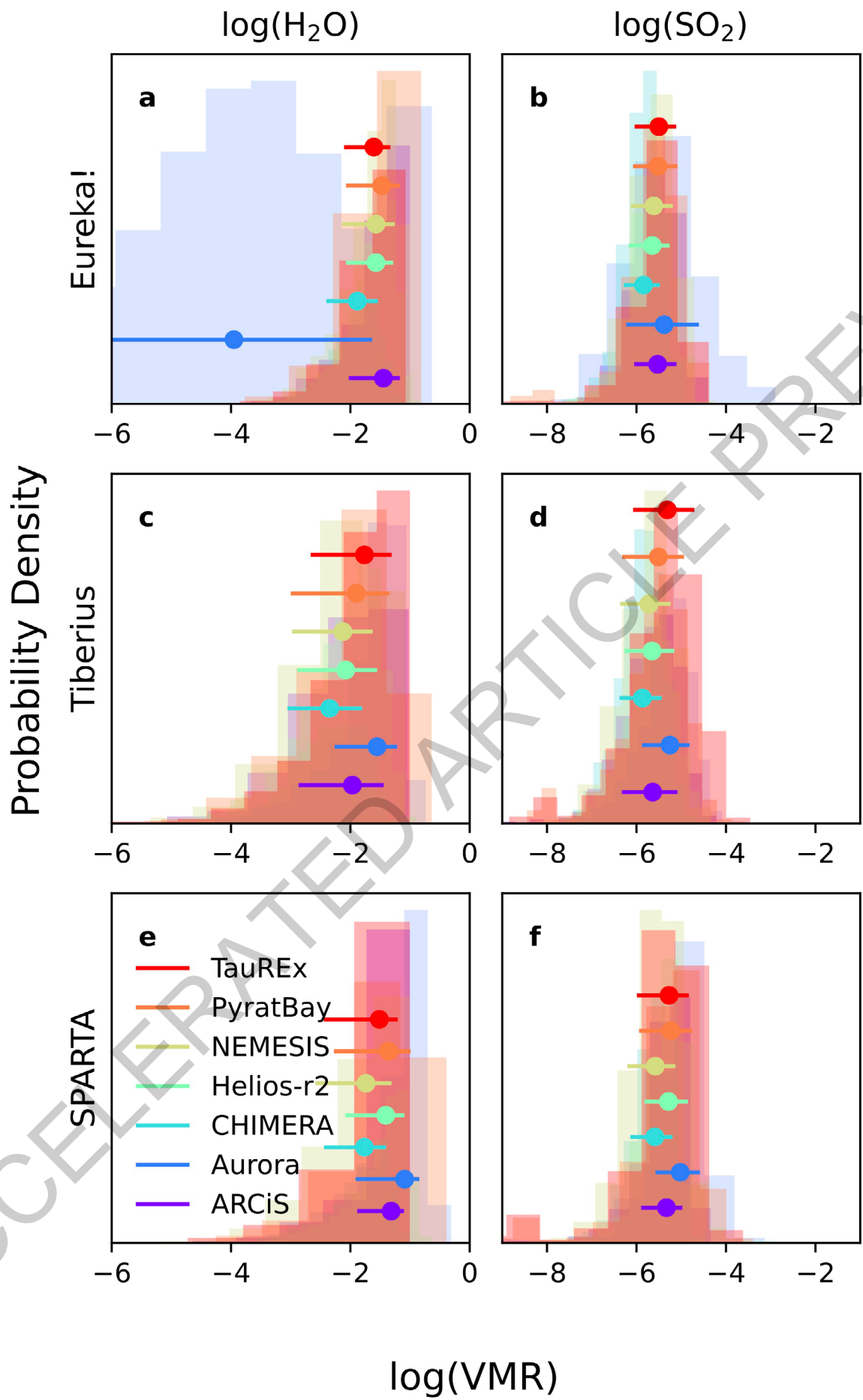
Extended Data Fig. 1



Extended Data Fig. 2



Extended Data Fig. 3



Extended Data Fig. 4

Reduction	T_0 (BJD _{TDB})	i (°)	a/R_*	R_P/R_*
Eureka!	2459990.320827 ± 0.000036	87.67 ± 0.04	11.34 ± 0.04	0.14531 ± 0.00021
Tiberius	2459990.320784 ± ^{0.000051} _{0.000052}	87.66 ± 0.08	11.31 ± 0.07	0.14523 ^{+0.00031} _{-0.00032}
SPARTA	2459990.320819 ± 0.000033	87.68 ± 0.05	11.35 ± 0.05	0.14522 ± 0.00024
(25)	2459791.6120684 ± ^{0.0000094} _{0.0000089}	87.7369 ± 0.0022	11.39 ± 0.012	—

Extended Data Table 1

Reduction	Best M*	χ^2	optimal M*
Eureka!	7.5	45.4	8.0 ± 1.1
Tiberius	7.5	16.4	7.1 ± 1.2
SPARTA	7.5	32.5	7.8 ± 1.2

Extended Data Table 2

Reduction	C^*_1	O^*_1	S^*_1	χ^2_1	C^*_2	O^*_2	S^*_2	χ^2_2	C^*_3	O^*_3	S^*_3	χ^2_3
Eureka!	1	18	1	36.7	1.8	18	1.0	37.0	1	30	1	37.1
Tiberius	1	13	1	14.7	1.8	13	1.0	14.7	1	7.5	1.8	14.8
SPARTA	1.0	56	1.0	27.0	5.6	30	1.0	37.0	3.0	30	1.0	27.1

Extended Data Table 3

	$\log(\text{H}_2\text{O})$	σ	$\log(\text{SO}_2)$	σ	Reduced χ^2	Cloud model
Eureka!						
ARCiS	$-1.5^{+0.3}_{-0.6}$	4.86	$-5.5^{+0.4}_{-0.5}$	3.59	1.54	grey, patchy
Aurora	$-3.9^{+2.3}_{-3.5}$	$\lesssim 2$	$-5.4^{+0.8}_{-0.9}$	3.39	1.06	haze + grey cloud, patchy
CHIMERA	$-1.9^{+0.4}_{-0.5}$	5.50	$-5.8^{+0.4}_{-0.5}$	3.96	1.24	haze + grey cloud, patchy
Helios-r2	$-1.6^{+0.3}_{-0.5}$	5.18	$-5.7^{+0.4}_{-0.5}$	2.54	1.77	grey
NEMESIS	$-1.6^{+0.3}_{-0.6}$	3.37	$-5.6^{+0.4}_{-0.5}$	3.35	1.54	grey, patchy
PyratBay	$-1.5^{+0.3}_{-0.6}$	2.58	$-5.5^{+0.5}_{-0.6}$	3.46	1.50	grey, patchy
TauREx	$-1.6^{+0.3}_{-0.5}$	3.09	$-5.5^{+0.4}_{-0.5}$	3.36	1.53	grey
Tiberius						
ARCiS	$-2.0^{+0.5}_{-0.9}$	3.95	$-5.6^{+0.6}_{-0.7}$	3.91	1.10	
Aurora	$-1.5^{+0.4}_{-0.5}$	3.82	$-5.3^{+0.5}_{-0.6}$	3.99	1.14	
CHIMERA	$-2.3^{+0.6}_{-0.7}$	4.62	$-5.9^{+0.4}_{-0.5}$	3.16	1.73	
Helios-r2	$-2.0^{+0.5}_{-0.8}$	4.38	$-5.7^{+0.5}_{-0.6}$	3.92	1.37	as above
NEMESIS	$-2.1^{+0.5}_{-0.9}$	4.74	$-5.7^{+0.5}_{-0.6}$	3.82	1.07	
PyratBay	$-1.9^{+0.6}_{-1.2}$	2.65	$-5.5^{+0.6}_{-0.9}$	4.21	1.12	
TauREx	$-1.8^{+0.5}_{-0.9}$	3.02	$-5.3^{+0.6}_{-0.8}$	3.92	1.08	
SPARTA						
ARCiS	$-1.3^{+0.2}_{-0.6}$	3.56	$-5.3^{+0.4}_{-0.6}$	3.36	1.15	
Aurora	$-1.1^{+0.2}_{-0.8}$	3.07	$-5.0^{+0.4}_{-0.6}$	2.95	0.95	
CHIMERA	$-1.8^{+0.7}_{-0.4}$	4.72	$-5.6^{+0.6}_{-0.4}$	3.11	1.29	
Helios-r2	$-1.4^{+0.3}_{-0.7}$	3.96	$-5.3^{+0.4}_{-0.5}$	2.99	1.36	as above
NEMESIS	$-1.7^{+0.4}_{-0.9}$	2.62	$-5.6^{+0.5}_{-0.6}$	3.11	1.20	
PyratBay	$-1.4^{+0.4}_{-1.0}$	2.98	$-5.3^{+0.5}_{-0.8}$	3.20	1.16	
TauREx	$-1.5^{+0.3}_{-0.9}$	2.75	$-5.3^{+0.4}_{-0.7}$	3.52	1.15	

Extended Data Table 4